JM PAPERS

Mathematical modelling of drying capillary porous media

Ellen K. Luckins[iD]

Mathematics Institute, Zeeman Building, University of Warwick, Coventry CV4 7AL, UK
Corresponding author: Ellen K. Luckins, ellen.luckins@warwick.ac.uk

The evaporation of liquid from within a porous medium is a complicated process involving coupled capillary flow, vapour diffusion and phase change. Different drying behaviour is observed at different stages during the process. Initially, liquid is drawn to the surface by capillary forces, where it evaporates at a near constant rate; thereafter, a drying front recedes into the material, with a slower net evaporation rate. Modelling drying porous media accurately is challenging due to the multitude of relevant spatial and temporal scales, and the large number of constitutive laws required for model closure. Key aspects of the drying process, including the net evaporation rate and the time of the sudden transition between stages, are not well understood or reliably predicted. We derive simplified mathematical models for both stages of this drying process by systematically reducing an averaged continuum multi-phase flow model, using the method of matched asymptotic expansions, in the physically relevant limit of slow vapour diffusion relative to the local evaporation rate (the large-Péclet-number limit). By solving our reduced models, we compute the evolving net evaporation rate, fluid fluxes and saturation profiles, and estimate the transition time to be when the initial constant-rate-period model ceases to be valid. We additionally characterise properties of the constitutive laws that affect the qualitative drying behaviour: the model is shown to exhibit a receding-front period only if the relative permeability for the liquid phase decays sufficiently quickly relative to the blow up in the capillary pressure as the liquid saturation decreases.

Key words: porous media, condensation/evaporation, capillary flows

1. Introduction

Drying of a liquid from within a porous medium is an important process to understand, with applications in soil science and geoscience, and industrially in the production of

1017 A6-1

paper, food and construction materials (Scherer 1990; Or *et al.* 2013; Wu & Prat 2022). Aside from the numerous applications, drying porous media are also extremely interesting from a fundamental fluid dynamics perspective, as a tightly coupled multi-phase and fluid–structure interaction system, with the multi-phase fluid flow and mass-transfer dynamics driven by the vaporisation and the transport mechanisms by which vapour is removed to the surroundings. Drying processes are challenging to model accurately due to the variety of relevant length scales and time scales over which processes occur: pore-scale capillary forces compete with viscous drag to generate large-scale flows, while macro-scale gradients in the vapour drive the evaporation.

In isothermal drying scenarios for which heat transfer may be neglected and when capillary forces play an important role, two main stages in the drying of a porous medium are typically observed. Firstly, during stage 1, liquid is drawn to the surface of the material by capillary flow and the evaporation takes place at or near the surface at a near-constant rate (stage 1 is often referred to as the 'constant-rate period' of the drying process). Stage 1 is seen to end abruptly when capillary forces are no longer sufficient to bring liquid to the surface. Thereafter, in stage 2, the net evaporation rate reduces significantly and continues to fall over time, as a drying front moves into the porous medium (stage 2 encompasses the 'falling-rate period' and 'receding-front period' referred to in some studies (Wu & Prat 2022)). Key aspects of the drying process – including determination of the 'constant' drying rate in stage 1 and the falling drying rate in stage 2, as well as the time and mechanism driving the transition to stage 2 – are not well understood and remain difficult to predict.

When capillary effects are important, drying porous media require an understanding of the multi-phase flow in porous media, with both phases (air and liquid) co-existing in the pore space. Many models for multi-phase flows in porous media focus on cases where the two fluids each saturate different regions of porous media and the sharp interface between these regions is sought as part of the model solution (e.g. Huppert & Woods 1995; Nordbotten & Celia 2006; Liu, Zheng & Stone 2017). Unsaturated flows are often modelled using the Richards equation (Richards 1931) and true multi-phase flows can be modelled with a multi-phase Darcy model (Bear 2013).

Models of drying of porous media consisting of saturated wet and dry regions separated by a sharp drying front are valid when capillary forces are negligible, and may also be reasonable when the material is hydrophilic (Luckins *et al.* 2023). When capillary forces are important in the drying of porous media, so the flow is truly multi-phase at the pore-scale, a range of different models have been used (Prat 2002; Vu & Tsotsas 2018; Li, Vanderborght & Smits 2019; Perré *et al.* 2023). The simplest of these are single (nonlinear) diffusion equations for the total moisture in the material, with the nonlinear diffusivity encompassing both liquid and vapour transport processes, and which is typically fit to experimental data (for instance, Pel & Landman 2004; Lockington, Parlange & Lenkopane 2007). Such simple models must be fit to specific drying scenarios and, even then, often fail to accurately capture the drying behaviour accurately (Whitaker 1977; Li *et al.* 2019). At the opposite extreme, the pore-scale multi-phase thermal Navier–Stokes equations may be averaged or homogenised to derive an averaged continuum model. These are multi-phase Darcy flow models, with mass transfer between phases, and often include an averaged heat transfer equation. In the drying literature, the averaged model of Whitaker (1977) is typically used. Due to the model complexity, it is typically solved numerically with purpose-built solvers (Wei *et al.* 1985; Perré & Turner 1999; Nuske, Joekar-Niasar & Helmig 2014; Li *et al.* 2019).

The benefit of averaged continuum models is their grounding in physical principles and, thus, the accuracy and interpretability of the results. The major drawbacks are their complexity and the large number of constitutive laws (or effective parameters) required to

close the model, including the relative permeabilities of each phase, the capillary pressure, the effective diffusivities and thermal conductivities, which typically vary with the local volume fraction of each fluid phase. Homogenisation methods are widely used, with great success, to provide closure problems for a variety of multi-scale systems, from which the effective parameters can be computed. However, for multi-phase flows in porous media (even when neglecting phase change), homogenisation methods are currently still unable to provide these closure problems in general (Lasseux & Valdés-Parada 2022) due to the significant dependence of the pore-scale problem on the pore geometry and flow history (Blunt 2017). In practice, for simulating the drying of porous media, the constitutive laws are often fixed by fitting to experimental data, or functional forms are posed based on their expected characteristics.

In addition to these continuum models, discrete pore network models (PNMs), describing the motion of liquid–gas interfaces through a network of pores representing the porous medium, are popularly used to study drying porous media (Metzger & Tsotsas 2010; Prat 2011). While these are still too computationally expensive to simulate the drying of an entire porous medium (Wu & Prat 2022), they are used to gain qualitative insight into drying scenarios and often to fix the constitutive laws required for the averaged continuum models (Ahmad *et al.* 2020).

Simplified or reduced versions of the averaged continuum models have been posed and simulated numerically. However, working solely with these simpler models has lead to significant confusion about their closure: topics of ongoing debate include how to impose appropriate boundary conditions on the reduced models (Talbi & Prat 2021; Wu & Prat 2022) and whether or not the assumption (often made) of local thermodynamic equilibrium is valid (Ouedraogo *et al.* 2013; Li *et al.* 2019; Ahmad *et al.* 2020).

In this paper, we use dimensional and asymptotic analysis to systematically simplify an isothermal, averaged continuum drying model (essentially that of Whitaker (1977)) in a relevant parameter regime, to derive new reduced models (and accompanying boundary conditions) for both stage 1 and stage 2 of the drying. We solve these reduced models to predict the stage-1 and stage-2 drying dynamics, including the net drying rates and receding front motion, as well as the time at which the transition between stages occurs.

There are several benefits to our asymptotic approach. Firstly, compared with simulating the full model of Whitaker (1977) numerically, our new, simple drying models provide powerful intuition, drawing out the fundamental force balances and fluid dynamics at play, and enabling the straightforward prediction of the drying rates and fluid velocities. Secondly, compared with the more *ad hoc* posing of reduced models in the existing drying literature, it is clear from our derivations the parameter regimes for which the reduced models are valid. Furthermore, our systematic analysis answers many questions about appropriate boundary conditions and regions of local equilibrium and out-of-equilibrium vaporisation kinetics currently debated in the drying literature. Importantly, much of our analysis is for general constitutive laws; we are therefore able to highlight where properties of the functional forms impact the qualitative drying behaviour, such as when (and even if) the system transitions from stage 1 to stage 2. This generality also enables us to identify the most important effective parameters to ascertain experimentally.

The remainder of the paper is structured as follows. In §2, we state the averaged continuum drying model following Whitaker (1977), discuss the required properties of appropriate constitutive laws and state physical boundary conditions. We then non-dimensionalise the model in §3 and discuss the parameter regimes of interest, before showing example numerical simulations of the model in §4. Section 5 is then focussed on one parameter regime of physical relevance, in which the vapour diffusion rate through the porous medium is slow relative to the local evaporation rate. Using the method of

matched asymptotic expansions, we derive and solve a reduced model for stage 1 (§ 5.1), predict the transition time (§ 5.2), and find and solve a reduced model for stage 2 (§ 5.3). We discuss and contextualise our results and provide concluding remarks in § 6.

2. Model statement

2.1. *An averaged continuum multi-phase model for isothermal drying*

We model the two-phase flow and phase change of the liquid and a mixture of vapour and inert gas (e.g. air) through a uniform-porosity porous medium using an averaged continuum model, as derived through volume averaging arguments by Whitaker (1977). Our starting point is the volume-averaged equations summarised in section VI of Whitaker (1977). The assumptions made in their derivation are also listed in that section. For our setting, the most important of these assumptions are that the liquid phase density is constant, the porous medium is homogeneous, the gas flow does not affect the liquid momentum balance except via the capillary pressure relation and that this capillary pressure is well defined. In particular, we emphasise that both the liquid and gas phases are assumed to be continuous. We further simplify this model of Whitaker (1977) by assuming that the porosity is constant, the drying process is isothermal (so that there is no temperature variation), the vapour–gas mixture has a constant intrinsic average density, and that the jump between the intrinsic averaged gas mixture and liquid pressures can be described by a capillary pressure. Under these assumptions, the dependent variables in our model are the liquid saturation, S (the volume fraction of liquid within the pore space, so that $1 - S$ is the volume fraction of the vapour–gas mixture within the pore space), the liquid and gas-mixture pressures, p^L and p^G, respectively, the liquid and gas-mixture Darcy fluxes, U^L and U^G, respectively, and the vapour mass density, ρ^v, within the gas phase. Specifically, ρ_v, p^G and p^L are the intrinsic average vapour density and fluid pressures (i.e. averaged only across the relevant phase). The model consists of Darcy's law and a conservation-of-mass constraint for each phase, incorporating the phase change with rate $\mathcal{M}$, an advection–diffusion equation for the transport of vapour and the assumed capillary pressure relation. The model is

$$U^L = -\frac{k_0}{\mu^L} k^L(S)\left(\nabla p^L + \rho^L g e_z\right), \tag{2.1a}$$

$$U^G = -\frac{k_0}{\mu^G} k^G(S)\left(\nabla p^G + \rho^G g e_z\right), \tag{2.1b}$$

$$\phi \rho^L S_t + \rho^L \nabla \cdot U^L = -\mathcal{M}(\rho^v, S), \tag{2.1c}$$

$$-\phi \rho^G S_t + \rho^G \nabla \cdot U^G = \mathcal{M}(\rho^v, S), \tag{2.1d}$$

$$\phi(1 - S)\rho_t^v + U^G \cdot \nabla \rho^v = D\nabla \cdot (D^{eff}(S)\nabla \rho^v) + \left(1 - \frac{\rho^v}{\rho_G}\right)\mathcal{M}(\rho^v, S), \tag{2.1e}$$

$$p^L = p^G - p_c(S), \tag{2.1f}$$

with subscript t denoting the partial derivative with respect to time t. Here, ϕ is the porosity, k_0 is the absolute permeability of the medium, ρ^L and ρ^G are the liquid and gas-mixture densities, D is the diffusivity of vapour in air through the dry porous medium, and μ^L and μ^G are the liquid and gas-mixture dynamic viscosities, all of which we assume to be constant. The liquid and gas-mixture phase pressures differ by the capillary pressure, $p_c(S)$, which we assume to be a known function of S. The relative permeabilities, $k^L(S)$ and $k^G(S)$, and the effective diffusivity through the gas-occupied pore space, $D^{eff}(S)$, are also assumed to be known functions of S only, while the mass-transfer rate between

the phases, $\mathcal{M}(\rho^v, S)$, is expected to depend on both the local vapour density and liquid saturation. Of course, all of these constitutive laws, p_c, k^L, k^G, D^{eff} and $\mathcal{M}$, additionally depend on the pore-scale geometry (sometimes encoded simply by a dependence on the porosity ϕ) and on the properties of the solid–liquid–gas combination, such as the contact angle of the contact lines. We assume the porous material to be homogeneous and the solid structure rigid and unchanging during the drying process, so that the dependence of the constitutive laws on these properties does not change during the course of the drying process. We explicitly include the constitutive laws' dependence on S and ρ^v since these vary spatially and temporally during the drying, as discussed in the following section.

2.2. *Constitutive relations*

As discussed previously, the form of the constitutive laws (or effective parameters) $p_c(S)$, $k^L(S)$, $k^G(S)$, $D^{eff}(S)$ and $\mathcal{M}(\rho^v, S)$ depend on the properties of the solid porous matrix, as well as the liquid and inert-gas pair considered. Expressions for some of these constitutive laws are given by Whitaker (1977), although these are difficult to evaluate explicitly as they are given in terms of the (unknown) microscale flow and transport. Others, such as $p_c(S)$ and $D^{eff}(S)$, do not follow from the volume averaging and must be determined empirically. Alternatively, upscaling via homogenisation methods typically results in more tractable methods by which the constitutive relations may be computed for a given pore geometry, although, as discussed in § 1, this is still only likely to be possible under strong restrictions on the pore geometry and phase distribution within the pore space, as in Lasseux & Valdés-Parada (2022). In practice, constitutive relations are often fit empirically or assumed based on heuristic arguments to solve models such as (2.1) numerically. In our analysis in § 5, we will leave the constitutive relations unfixed as far as is possible to maintain generality and investigate how the qualitative behaviour of the drying system depends on the properties of their functional forms. Indeed, we will later show that the choice of these functional forms can strongly affect the type of drying behaviour observed. In this section, we discuss the typical properties of the constitutive laws and some simple examples.

Generally, we require that p_c is a monotonic decreasing function of S, with $p_c = 0$ at $S = 1$ and $p_c \to \infty$ as S becomes small. The relative permeabilities of each phase should be an increasing function of the volume fraction of that phase, so that $k^L(S)$ is increasing and $k^G(S)$ is decreasing, with $k^L(1) = k^G(0) = 1$ and $k^L(0) = k^G(1) = 0$. In reality, there may be significant hysteresis between wetting and drying regimes, due to the history dependence of the pore-scale flow (Blunt 2017). Since we are interested only in drying, we will assume a single relation for each of $p_c(S)$, $k^L(S)$, $k^G(S)$. Commonly used forms with these properties include

$$k^L(S) = S^a, \qquad k^G(S) = (1-S)^b, \qquad p_c(S) = S^{-c} - S^d, \qquad (2.2)$$

for some powers a, b, c, $d > 0$ (Fowler 2011; Blunt 2017). The model of Van Genuchten (1980) is also popular in simulating drying (Ouedraogo *et al.* 2013; Li *et al.* 2019). We will keep the constitutive laws general as much as possible through our analysis, but for examples and simulations, will use (2.2) with $a = b = 3$ and $c = d = 1$ (Fowler 2011) unless otherwise stated.

The evaporation rate $\mathcal{M}$ is also assumed to be some known function of ρ^v and S. From the volume-averaging argument, we might expect to be able to decompose

$$\mathcal{M} = \mathcal{A}(S) E(\rho^v, S), \qquad (2.3)$$

where $\mathcal{A}(S)$ is a measure of the surface area to volume ratio of the liquid–gas interface on the microscale and $E(\rho^v, S)$ is the local evaporative flux rate on the microscale. This

$\mathcal{A}(S)$ is sometimes referred to as the specific interfacial area of the surface in the drying literature (Ahmad *et al.* 2020; Wu & Prat 2022). Ahmad *et al.* (2020) used simulations of a pore-network model to approximate $\mathcal{A}(S)$, and found for their simulations that $\mathcal{A} \to 0$ as $S \to 0$ and $\mathcal{A}$ was non-monotone in S. The local evaporation rate is often taken to be linear in the vapour density ρ^v (or equivalently, since we assume an isothermal system, in the vapour partial pressure). An example of such a linear model for E is a Hertz–Knudsen law (Hertz 1882)

$$E(\rho^v) = C(\rho_*^v - \rho^v), \tag{2.4}$$

for constant C (usually inversely proportional to the temperature), and where ρ_*^v is the saturation vapour density. As well as the local vapour density, the local rate E might also depend on the liquid–gas interface curvature and, therefore, the pore-scale geometry of the porous medium. It is for this reason that E may also depend on the saturation S, as a proxy for this pore-scale geometry dependence. In general, E might depend on surface adsorption or dual-porosity effects, which could also be modelled via a dependence on S. We will assume throughout that the porous medium is simple and non-reactive with the liquid – for instance, an array of glass beads – and therefore that E is independent of S.

The effective diffusivity $D^{eff}(S)$ of vapour through the porous medium is expected to decrease with S as the pore-volume occupied by the gas mixture is reduced. We require $D^{eff}(1) = 0$ and $D^{eff}(0) = 1$ (the effective diffusivity of vapour through the porous medium with no liquid present has been incorporated into the dimensional constant D). In general, the form of $D^{eff}(S)$ will also depend on the pore-scale geometry (Bruna & Chapman 2015) but for simplicity, we will take $D^{eff}(S) = (1 - S)^{1/2}$ in numerical simulations, unless otherwise stated.

2.3. *Problem of interest and appropriate boundary conditions*

In this paper, we consider drying from an effectively one-dimensional porous medium with an impermeable base at $z = 0$ and open to the surrounding air at the top, $z = L$, so that L is the depth of the porous medium. (If there were no gravitational effect, this geometry also captures the symmetric drying of a porous medium between $z = (-L, L)$, with a line of symmetry at $z = 0$.) While the porous medium is in reality three-dimensional, by imposing initial and boundary conditions that are independent of x and y, we expect the dependent variables to only depend on z spatially. Furthermore, the drying process, which we will see is limited by diffusion of vapour out of the material, is expected to be stable, and thus we do not anticipate higher dimensional effects becoming important.

By eliminating U^L, U^G (the z-directional scalar Darcy fluxes) and p^L using (2.1a), (2.1b) and (2.1f), our model may be viewed as three, spatially second-order, (diffusive) equations for S, p^G and ρ^v. We therefore require one boundary condition on each of S, p^G and ρ^v at each edge of the domain, $z = 0$ and $z = L$, as well as a consistent initial condition for each of these three variables.

At the impermeable base, we impose no flux of liquid, gas or vapour, so that

$$U^L = U^G = D D^{eff} \rho_z^v = 0 \qquad \text{at } z = 0. \tag{2.5}$$

Here, we use subscript z to denote derivative with respect to z. These conditions (2.5) may be interpreted as corresponding to one condition on each of S, p^G and ρ^v, respectively.

At the surface of the material, there can be no flux of liquid out of the material and the gas pressure is atmospheric, so that

$$U^L = 0, \quad p^G = p_{atm}^G \qquad \text{at } z = L. \tag{2.6}$$

These may be viewed as one boundary condition on each of S and p^G. The final boundary condition for ρ_v on $z = L$ depends on how vapour is transported through the surrounding air. Most generally, we might couple the drying porous medium with a model for the external vapour transport. For simplicity, we consider two simpler alternatives. First, we might impose that the vapour density is at a constant value, an atmospheric humidity, at the top of the porous medium, so that

$$\rho^v = \rho^v_\infty \qquad \text{at } z = L, \tag{2.7}$$

which is valid if the vapour is very quickly removed from the surface of the porous medium, for instance, if there is a fast flow of dry air across it. Alternatively, we might impose a mass flux or Newton-cooling law, with a mass transfer coefficient m, so that the flux of vapour out of the top of the porous medium is given by

$$\rho^v U^G - D D^{eff} \rho^v_z = m(\rho^v - \rho^v_\infty) \qquad \text{at } z = L. \tag{2.8}$$

In the limit of fast mass transfer through the surrounding air, $m \to \infty$, this mass-flux boundary condition (2.8) reduces to the Dirichlet condition (2.7). Either of (2.7) or (2.8) completes the set of boundary conditions on the model.

Initially, we will assume known saturation, vapour density and gas pressure profiles. Typically, we might assume these are uniform with $S = S_0 < 1$, $p^G = p^G_{atm}$ and $\rho^v = \rho^v_\infty$.

The correct boundary conditions to impose at the surface of a drying porous medium are widely debated in the drying literature, especially in relation to simplified continuum models for which the liquid and vapour are assumed to be in local equilibrium (so $\rho^v = \rho^v_*$ throughout), or the conservation of mass equations are combined into a single diffusive equation for the saturation (Li *et al.* 2019; Talbi & Prat 2021; Wu & Prat 2022). The conditions stated previously, (2.6) and either of (2.7) or (2.8), are physically motivated and by systematically reducing our model in § 5, we derive the corresponding boundary conditions for our simplified models. It will be clear what the correct boundary conditions should be for our reduced models because they are the appropriate reduction of the boundary conditions for the above mentioned full model.

3. Non-dimensionalisation

We now non-dimensionalise our model. We impose the length scale, L, of the porous medium, the pore-length scale, d, (we assume throughout that $\epsilon = d/L \ll 1$) and the evaporation rate scaling, $[E]$, but otherwise choose the scalings that are due to the evaporation process, since all flow and transport is driven by the evaporation.

Arguing geometrically, we expect the liquid–gas interface area to volume ratio to scale like $\mathcal{A}(S) \sim 1/d$. We suppose that from E, we know the characteristic saturation vapour density ρ^v_*; at $\rho^v = \rho^v_*$, $E = 0$, and physically relevant solutions have $\rho^v \leqslant \rho^v_*$. We also suppose we know the characteristic scaling $[E]$ for the evaporation rate E. For instance, if E were the Hertz–Knudsen law (2.4), then we could take $[E] = C\rho^v_*$. Since we will later focus on the situation where vapour diffusion limits the evaporation, it is in fact helpful to scale

$$\mathcal{M} \sim \nu \frac{[E]}{d}, \qquad \text{where } \nu = \frac{\rho^v_*}{\rho^G}, \tag{3.1}$$

and so account for the maximum humidity, ν, within the scaling for the mass transfer term. The capillary pressure scales with the surface tension γ and interface curvature, and thus, $p_c \sim \gamma/d$. This is also known as the pore-entry pressure.

In summary, we make the rescalings

$$\mathcal{M} = \frac{v[E]}{d}\tilde{E}(\tilde{\rho}, S)\tilde{\mathcal{A}}(S), \qquad p_c(S) = \frac{\gamma}{d}\tilde{p}_c(S), \qquad (3.2a)$$

as well as

$$t = \frac{\phi\rho^L d}{v[E]}\tilde{t}, \qquad \boldsymbol{U}^L = \frac{v[E]L}{d\rho^L}\tilde{\boldsymbol{U}}^L, \qquad \boldsymbol{U}^G = \frac{v[E]L}{d\rho^G}\tilde{\boldsymbol{U}}^G, \qquad (3.2b)$$

$$p^L = p_{atm} + \frac{\gamma}{d}\tilde{p}^L, \qquad p^G = p_{atm} + \frac{\gamma}{d}\tilde{p}^G, \qquad \rho^v = \rho_*^v\tilde{\rho}, \qquad (3.2c)$$

so that the time scale is that of the local evaporation rate, the gas and liquid flow velocities are driven by the evaporation, and the pressures scale with the capillary pressure.

Using the scalings (3.2) and dropping the tilde notation for dimensionless variables, we find the dimensionless model,

$$\boldsymbol{U}^L = -Ca^{-1}k^L(S)\big(\boldsymbol{\nabla}p^L + Bo\,\boldsymbol{e}_z\big), \qquad (3.3a)$$

$$\boldsymbol{U}^G = -\xi Ca^{-1}k^G(S)\big(\boldsymbol{\nabla}p^G + \delta Bo\,\boldsymbol{e}_z\big), \qquad (3.3b)$$

$$S_t + \boldsymbol{\nabla}\cdot\boldsymbol{U}^L = -\mathcal{A}(S)E(\rho), \qquad (3.3c)$$

$$-\delta S_t + \boldsymbol{\nabla}\cdot\boldsymbol{U}^G = \mathcal{A}(S)E(\rho), \qquad (3.3d)$$

$$v\delta(1-S)\rho_t + v\boldsymbol{U}^G\cdot\boldsymbol{\nabla}\rho = Pe^{-1}\boldsymbol{\nabla}\cdot\big(D^{eff}(S)\boldsymbol{\nabla}\rho\big) + (1-v\rho)\,\mathcal{A}(S)E(\rho), \qquad (3.3e)$$

$$p^L = p^G - p_c(S), \qquad (3.3f)$$

where we have introduced the dimensionless parameters

$$\delta = \frac{\rho^G}{\rho^L}, \qquad v = \frac{\rho_*^v}{\rho^G}, \qquad \xi = \frac{\rho^G\mu^L}{\rho^L\mu^G}, \qquad (3.4a)$$

$$Bo = \frac{\rho^L gLd}{\gamma}, \qquad Ca = \frac{L^2\mu^L v[E]}{k_0\rho^L\gamma}, \qquad Pe = \frac{[E]L^2}{D\rho^G d}. \qquad (3.4b)$$

For the one-dimensional problem of interest stated in §2.3, the dimensionless boundary conditions are

$$\boldsymbol{U}^L = \boldsymbol{U}^G = D^{eff}\rho_z = 0 \qquad \text{on } z = 0, \qquad (3.5a)$$

$$\boldsymbol{U}^L = p^G = 0 \qquad \text{on } z = 1, \qquad (3.5b)$$

$$\text{either} \quad v\boldsymbol{U}^G\rho - Pe^{-1}D^{eff}\rho_z = m(\rho - \rho_\infty) \quad \text{or} \quad \rho = \rho_\infty \qquad \text{on } z = 1, \qquad (3.5c)$$

(with m and ρ_∞ rescaled as appropriate) and initially, we prescribe uniform initial profiles $S = S_0$, $\rho = 1$, and zero fluxes and pressure gradients. The density ratio δ, humidity v and kinematic viscosity ratio, ξ, are all expected to be small. The Bond number Bo quantifies the effect of gravity on the liquid relative to the capillary forces with $Bo \ll 1$ (true for sufficiently small length scales d or L) corresponding to minimal gravitational effect, while $Bo \gg 1$ corresponds to gravity forces dominating. Since our focus is capillary porous media, we will be interested primarily in the case $Bo \ll 1$. The capillary number Ca is the ratio of viscous drag force in the pore space to the capillary forces, so that $Ca \ll 1$ corresponds to strong capillary forces. The absolute permeability k_0 can vary by several orders of magnitude for different porous media and is often taken to scale approximately with d^2. Finally, the Péclet number, Pe, may be thought of as the ratio of the local evaporative flux rate to the rate of diffusive transport of the vapour through the porous medium, so that $Pe \gg 1$ corresponds to the situation of drying limited by the transport of vapour out of the porous medium, and we expect the liquid and vapour to be in

Parameter	Description	Approximate value or range
ρ^G	Gas density	$1 \, \mathrm{kg \, m^{-3}}$
ρ^L	Liquid density	$10^3 \, \mathrm{kg \, m^{-3}}$
ρ_*^v	Saturation vapour density	$2 \times 10^{-2} \, \mathrm{kg \, m^{-3}}$
μ^L	Liquid viscosity	$10^{-3} \, \mathrm{kg \, m^{-1} s^{-1}}$
μ^G	Gas viscosity	$2 \times 10^{-5} \, \mathrm{kg \, m^{-1} \, s^{-1}}$
γ	Surface tension	$7.2 \times 10^{-2} \, \mathrm{kg \, s^{-2}}$
D	Diffusivity of vapour in air	$2.5 \times 10^{-5} \, \mathrm{m^2 \, s^{-1}}$
d	Pore length scale	$10^{-5} \, \mathrm{m}$
L	Porous medium length scale	$5 \times 10^{-2} \, \mathrm{m}$
k_0	Absolute permeability	$10^{-11} \, \mathrm{m^2}$
$[E]$	Kinetic evaporation rate	$2.5 \times 10^{-3} \, \mathrm{kg \, m^{-2} \, s^{-1}}$

Table 1. Approximate parameter values for the drying of water from a capillary porous medium, in air, at room temperature.

Dimensionless parameter	Estimated value	Value used in numerical simulations
δ	10^{-3}	10^{-3}
ν	2×10^{-2}	2×10^{-1}
ξ	5×10^{-2}	5×10^{-1}
Bo	6.8×10^{-2}	0
Ca	1.7×10^{-1}	Various
Pe	2.5×10^4	Various

Table 2. Dimensionless parameter values using the data in table 1 for the estimates. We will use less extreme values of several parameters in our numerical simulations to aid computational efficiency, while remaining in the relevant limits.

thermodynamic equilibrium. We note that all of Bo, Ca and Pe increase with the material thickness L and also vary with the pore-length scale d (scaling $k_0 \sim d^2$).

In table 1, we list data values relevant for the drying of water at room temperature in a capillary porous medium and the corresponding dimensionless parameters are listed in table 2. Since δ is small, the gas and vapour equations are likely to be stiff to simulate, and we should expect quasi-steady gas and vapour dynamics on the evaporation time scale (so long as the saturation is not too close to 1, in which case, the time derivative terms in (3.3d)–(3.3e) would become important (Murphy 2024). The parameters ν and ξ are also fairly small, although we will often be able to retain generality by treating them as $O(1)$ through much of our analysis.

Since $Pe \gg 1$ and $Ca \ll 1$, we expect the drying to be limited by diffusion of vapour through the porous medium and that the capillary forces will dominate over viscous drag.

With the data in table 1, the time scale that we have used is

$$[t] = \frac{\phi \rho^L d}{\nu [E]} \approx 10^3 \, \mathrm{s}, \tag{3.6}$$

which is the time scale associated with the evaporation rate. We will later see that for $Pe \gg 1$, vapour transport limits the drying process and the time scale for the constant rate
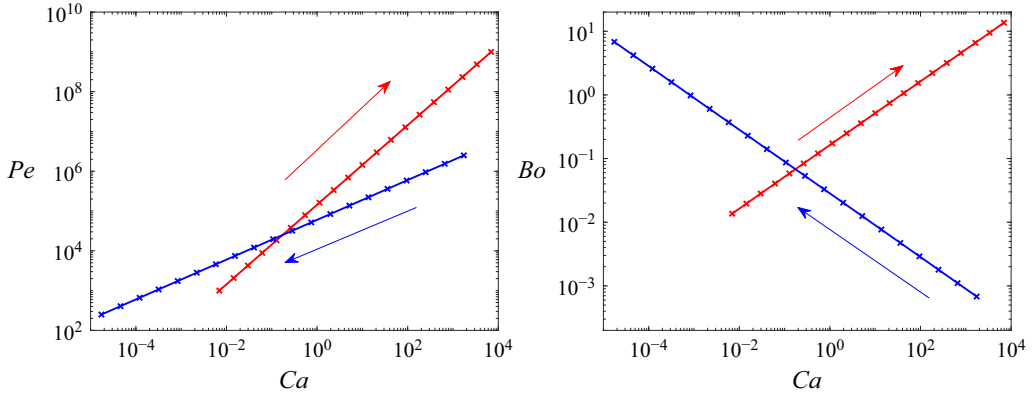
Figure 1. Variation of the capillary, Péclet and Bond numbers with the pore-length scale d (curves in blue, arrows show direction of increasing d) and the size of the porous medium L (similarly in red). Along blue curves, d varies from 10^{-7} m to 10^{-3} m and we take $k_0 = 0.1d^2$ m^2; along red curves, L varies from 10^{-2} to 10 m. All parameters are as in table 1 unless otherwise stated.

drying during stage 1 is actually longer than this, on the order of

$$[t]\sqrt{Pe} \approx 1.6 \times 10^4 \text{ s} \approx 4.4 \text{ h}, \tag{3.7}$$

a reasonable drying time scale for the chosen length scales.

In figure 1, we show the variation of Pe, Ca and Bo with d and L, over reasonable sizes that might be of interest. Whilst the Bond and capillary numbers might be large or small in certain cases, the Péclet number is generally large. In § 5, we investigate this large Péclet limit of interest.

4. Numerical method and typical solutions

To solve (3.3) numerically, in one spatial dimension ($z \in (0, 1)$), we eliminate U^L and U^G by substituting Darcy's laws into the other equations, and eliminate $p^L = p^G - p_c(S)$. Thus, we have three coupled equations for S, ρ and p^G, namely

$$S_t - Ca^{-1}\big(k^L(S)\big(p_z^G - p_c'(S)S_z + Bo\big)\big)_z = -\mathcal{A}(S)E(\rho), \tag{4.1a}$$

$$-\delta S_t - \xi Ca^{-1}\big(k^G(S)\big(p_z^G + \delta Bo\big)\big)_z = \mathcal{A}(S)E(\rho), \tag{4.1b}$$

$$\delta\nu(1-S)\rho_t - \nu\xi Ca^{-1}k^G(S)\big(p_z^G + \delta Bo\big)\rho_z = Pe^{-1}\big(D^{eff}(S)\rho_z\big)_z + (1-\nu\rho)\mathcal{A}(S)E(\rho). \tag{4.1c}$$

We solve these subject to the boundary conditions (3.5), taking the Dirichlet condition

$$\rho = \rho_\infty \qquad \text{at } z = 1. \tag{4.2}$$

There are two time derivatives of the saturation, S_t, in the system (4.1), and none of the gas pressure p^G. We therefore solve (4.1a) and (4.1c) for S and ρ, while at every time step, the gas pressure p^G is related to S and ρ via the spatial ordinary differential equation (ODE)

$$-Ca^{-1}\big(\delta k^L(S)\big(p_z^G - p_c'(S)S_z + Bo\big) + \xi k^G(S)\big(p_z^G + \delta Bo\big)\big)_z = (1-\delta)\mathcal{A}(S)E(\rho), \tag{4.3}$$

which is derived by eliminating S_t between (4.1a)–(4.1b).

We solve (4.1*a*), (4.1*c*) and (4.3), with the boundary conditions (3.5*a*), (3.5*b*) and (4.2) using the method of lines, with finite-differences for the spatial derivatives. Specifically, we use a second-order central difference scheme for diffusive terms and a first-order upwind scheme where required for advective terms. The resulting system of temporal ODEs is solved in MATLAB using the inbuilt multi-step solver ode15s, which is specialised to retain efficiency for stiff systems (Shampine & Reichelt 1997) to an absolute and relative tolerance of 10^{-6} and 10^{-3}, respectively. Since δ and ν are small, we expect significant stiffness in our system, especially from the vapour transport equation (4.1*c*) with a time-derivative multiplied by $\delta\nu \approx 10^{-5}$ for physical values in table 2. For numerical efficiency, we will typically use ν and ξ values an order of magnitude larger than estimated, as stated in table 2. Similarly, for large Pe, a fine spatial mesh is needed to accurately capture the behaviour in thin regions of the domain (of typical width $O(Pe^{-1/2})$, as we will see in § 5). For this reason, we use less extreme values of Pe than that estimated in table 2 in our numerical simulations, which require a more moderate mesh-size of around 250 mesh points.

A solution of (4.1*a*), (4.1*c*) and (4.3), with the boundary conditions (3.5*a*), (3.5*b*) and (4.2), computed numerically in this way, is shown in figure 2. Here, we have set $Bo = 0$ so there is no gravitational effect, and chosen $Ca = 1$ and $Pe = 1000$. We use the constitutive laws $k^L(S) = S^3$, $k^G(S) = (1 - S)^3$, $p_c(S) = 1/S - S$, $\mathcal{A}(S) = 1/2$, $D^{eff}(S) = (1 - S)^{1/2}$ and $E(\rho) = 1 - \rho$. In figure 2(*a*), we show the net evaporation rate, defined to be

$$\text{net evaporation rate} = \int_{z=0}^{1} \mathcal{A}(S) E(\rho) \, \mathrm{d}z, \tag{4.4}$$

as a function of time t. After a fast $O(\nu\delta)$ initial transient (while the vapour density ρ attains its quasi-steady profile from the initial condition), we observe two distinct regions, separated by a red-dotted line at the critical time $t = t_* \approx 20$. First we see stage-1 drying, where the evaporation rate is nearly constant. (In this case, we actually observe the net evaporation rate increases slightly over time; in § 5.1, we show that this is due to the choice of $\mathcal{A}(S)$ and $D^{eff}(S)$). Near to t_*, there is a sharp transition to stage-2 drying, where the net evaporation rate is significantly lower and falls over time. The drying is complete in this simulation by time $t = 41$.

In figure 2(*b–f*), we show the spatial profiles of S, ρ, p^G, U^L and U^G, respectively, at equally spaced time-points through the drying process. Those in stage 1 (for $t < t_*$) are black, while those in stage 2 ($t > t_*$) are shown in blue. We additionally show the profiles at $t = t_*$ in red. In figure 2(*b*), we see that during stage 1, the saturation is roughly uniform, although S decreases slightly towards the top of the porous medium at $z = 1$. We clearly see that the transition between stage-1 and stage-2 drying occurs at the point where $S = 0$ at $z = 1$; in stage 2, there is no longer liquid at the surface of the porous medium and the drying front recedes into the material so that vaporisation occurs within the material. During stage 1, we see in figure 2(*c*) that the vapour density is at its saturation point $\rho = 1$ and in figure 2(*f*), the gas velocity is zero through the majority of the material, only varying within a thin layer at the surface $z = 1$. In stage 2, we see a roughly linear vapour density profile and a constant gas velocity in the dry region of the domain. The liquid velocity U^L, shown in figure 2(*e*), is positive as liquid is drawn up to (in stage 1) and towards (in stage 2) the surface of the porous medium. We note that the dimensionless liquid and gas velocities, and the gas pressure are all fairly small. This is because the net evaporation rate is small, as we will show in § 5.

The solution shown in figure 2 bears strong qualitative resemblance to experimental results (e.g. Pel, Brocken & Kopinga 1996; Gupta *et al.* 2014) and is characteristic of the
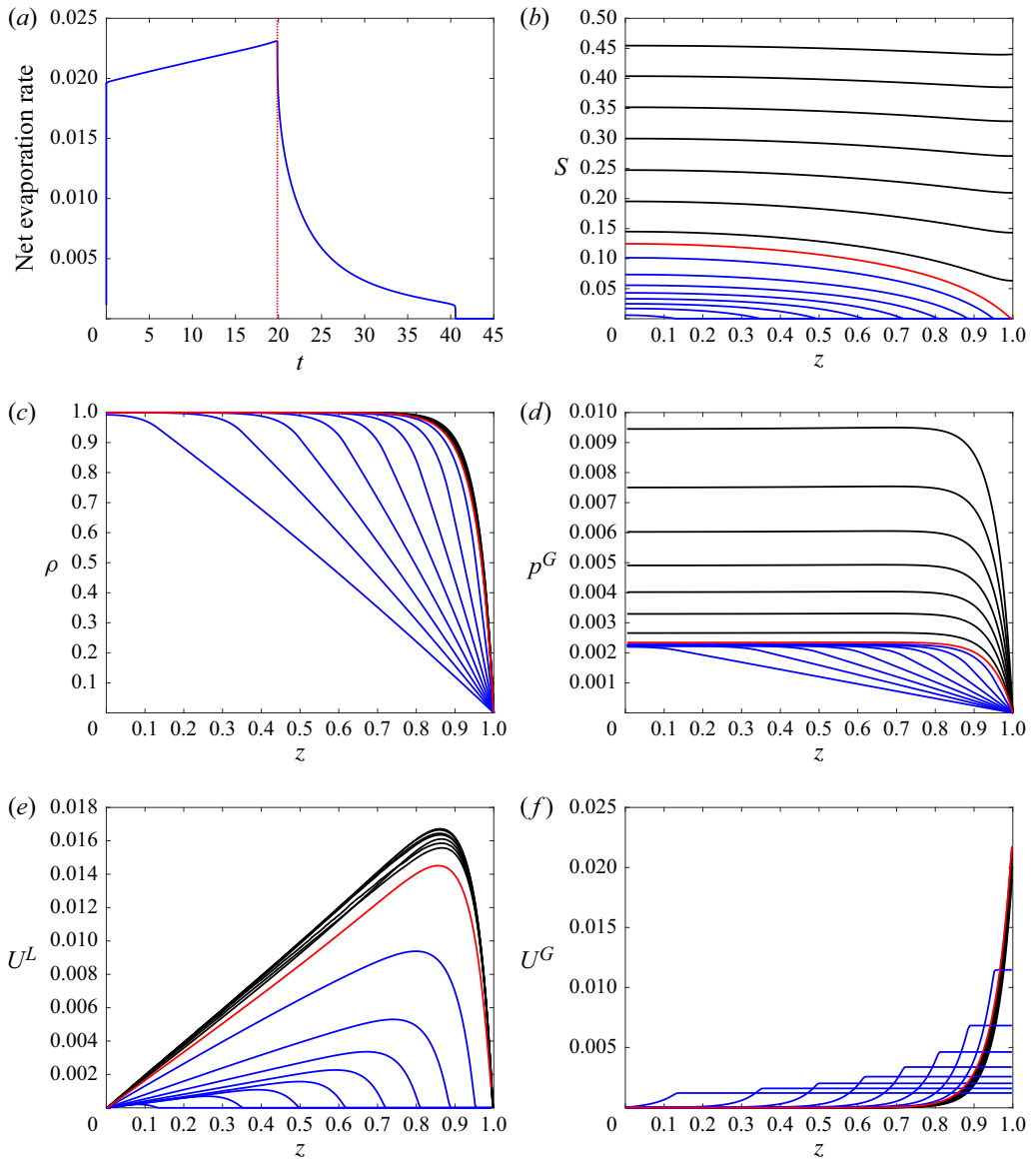
Figure 2. Numerical solution of (3.3), with $Pe = 1000$, $Ca = 1$, $Bo = 0$, $\rho_\infty = 0$ and all other parameters as in table 2. Initially, $S = 0.5$, $\rho = 1$. Profiles in panels (*b–d*) are at equally spaced times $t = $ [2.67, 5.34, 8.02, 10.7, 13.4, 16.0, 18.7, 21.4, 24.0, 26.7, 29.4, 32.1, 34.5, 37.4, 40.1], with black curves during stage 1 ($t < t_* \approx 19.9$) and blue curves during stage 2 ($t > t_*$), with the addition of a red curve at the transition time $t_* = 19.9$.

large-Pe drying scenarios we will investigate further in this paper. It exhibits many of the features we aim to understand and be able to predict, including the net evaporation rate, and the transition time between stages 1 and 2. Our model (3.3) and numerical method are valid for a much wider parameter regime than the case shown (with $Pe \gg 1$, $Bo \ll 1$ and moderate Ca), although exploration of these alternative regimes is beyond the scope of the present study.
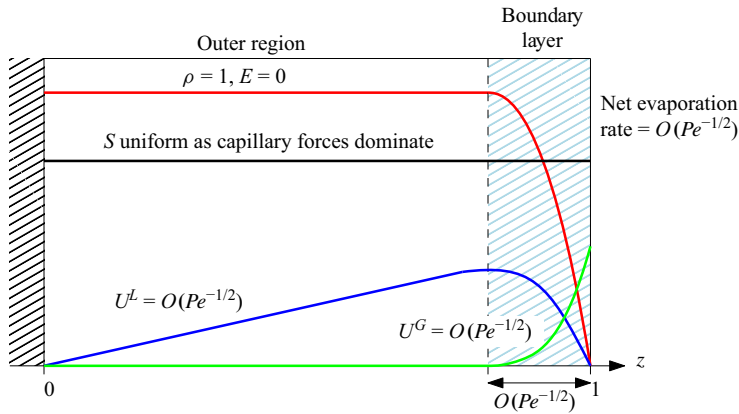
Figure 3. Schematic illustrating the solution structure during stage 1.

5. The large-*Pe* limit

For the remainder of the paper, we consider in detail the limit of large Péclet number $Pe \gg 1$. This means that the (diffusive) transport of vapour out of the material is slow relative to the rate of evaporation and so vapour transport limits the drying.

We also assume for the analysis in this section that $\delta \ll 1$, $Bo \ll 1$ so that gravity has little effect, and that the capillary number is not too large in the specific sense that $Ca \ll \max(\xi Pe, \sqrt{Pe})$. This ensures that capillary forces are dominant in the fluid flows and is not too restrictive since we are assuming that $Pe \gg 1$. Recalling the discussion of § 3, this set of assumptions is valid for sufficiently small d and L.

5.1. *Stage 1: the 'constant rate period'*

Since $Pe \gg 1$, we see from (3.3e) that the evaporation rate is zero and the vapour density must take its saturation value $\rho = 1$ everywhere except in a thin boundary layer, of width $1/\sqrt{Pe} \ll 1$, at the surface $z = 1$ of the porous medium (this boundary-layer width is determined by a balance in (3.3e)). Since evaporation only occurs in this thin boundary-layer region, we see from (3.3c)–(3.3d) that there can be at most an $O(1/\sqrt{Pe})$ flow generated in either fluid. The time scale of the drying is determined by the time scale of changing saturation over the entire domain. Balancing the two terms on the left of (3.3c) over the $O(1)$ length scale, we see that the time scale is longer, $O(\sqrt{Pe})$, since the flux of liquid is smaller. This is intuitive, since evaporation only takes place in a thin layer, so the time taken to evaporate all of the liquid must be proportionately longer. A schematic diagram illustrating the structure of the solution in stage 1 is shown in figure 3.

Motivated by these scaling choices, to study stage 1, we make the change of variables

$$t = \sqrt{Pe}\,\tau, \qquad U^G = \frac{1}{\sqrt{Pe}} V^G, \qquad U^L = \frac{1}{\sqrt{Pe}} V^L. \qquad (5.1)$$

5.1.1. *Outer region*
On an $O(1)$ length scale and with the rescalings (5.1), the model (3.3) then becomes

$$CaPe^{-1/2}V^L = -k^L(S)\big(p_z^L + Bo\big), \tag{5.2a}$$

$$\xi^{-1}CaPe^{-1/2}V^G = -k^G(S)\big(p_z^G + \delta Bo\big), \tag{5.2b}$$

$$Pe^{-1/2}\big(S_\tau + V_z^L\big) = -\mathcal{A}(S)E(\rho), \tag{5.2c}$$

$$Pe^{-1/2}\big(-\delta S_\tau + V_z^G\big) = \mathcal{A}(S)E(\rho), \tag{5.2d}$$

$$Pe^{-1/2}\big(\delta\nu(1-S)\rho_\tau + \nu V^G\rho_z\big) = Pe^{-1}\big(D^{eff}(S)\rho_z\big)_z + (1-\nu\rho)\mathcal{A}(S)E(\rho). \tag{5.2e}$$

We see from (5.2e) that

$$O\big(Pe^{-1/2}\big) = (1-\nu\rho)\,\mathcal{A}(S)E(\rho). \tag{5.3}$$

Thus, since $\rho \leqslant 1$, $\nu < 1$ and $S > 0$, we must have that the vapour density is at its saturation value $\rho = 1$, so that $E = 0$ to leading order in $Pe^{-1/2}$. Indeed, looking for an $O(Pe^{-1/2})$ correction to ρ in (5.2e) results in that correction being zero (since the leading-order $\rho = 1$ has no derivatives) and, arguing inductively in this way, over an order 1 length scale, we see that

$$\rho = 1 - \text{ exponentially small correction.} \tag{5.4}$$

Since the evaporation rate is therefore exponentially small, from (5.2d), along with the assumption that $\delta \ll 1$, we must have a uniform gas flux $V_z^G = 0$ and so, using the boundary condition $V^G = 0$ at $z = 0$, we see that

$$V^G = 0, \tag{5.5}$$

while from (5.2c), we find that

$$S_\tau + V_z^L = 0. \tag{5.6}$$

Since $V^G = 0$, so long as $\delta Bo \ll 1$, then from (5.2b), we must have a uniform gas pressure $p_z^G = 0$ through the outer region.

Furthermore, if $Ca \ll Pe^{1/2}$ and $Bo \ll 1$, then from the liquid Darcy law (5.2a), we see that, since the liquid flow is slow, the liquid pressure $p^L = p^G - p_c(S)$ is also uniform to leading order. Thus, we must have the expected uniform (although time-varying) saturation, S, throughout this outer region.

This uniform saturation profile simplifies the problem greatly. By integrating (5.6) over the outer region, we see that the rate of change of saturation,

$$S_\tau = -\big[V^L\big]_0^1 = -V^{L,BL}, \tag{5.7}$$

is precisely the flow of liquid $V^{L,BL}$ into the boundary layer at the surface. Furthermore, since S_τ is independent of z, the liquid flux,

$$V^L = -S_\tau z = V^{L,BL}z, \tag{5.8}$$

is linear in z.

In summary, at leading order through the outer region, there is no evaporation and no gas flow, the saturation, vapour density and gas pressure are all uniform (with the vapour density at its saturation point 1), and the liquid flux is linear in z, determined by the rate at which liquid is drawn into the boundary layer. To understand the flow rate $V^{L,BL}$ into the boundary layer, we must examine the boundary-layer processes in more detail.

5.1.2. *Boundary layer at $z = 1$*

In addition to the scalings (5.1), within the boundary layer at $z = 1$, we set

$$z = 1 + \frac{1}{\sqrt{Pe}} X, \tag{5.9}$$

noting that the top of the porous medium at $z = 1$ is at $X = 0$, and as $X \to -\infty$, we leave the boundary layer and enter the outer region. In the boundary layer, (3.3) become

$$Ca Pe^{-1} V^L = -k^L(S) \left(p_X^L + Pe^{-1/2} Bo \right), \tag{5.10a}$$

$$\xi^{-1} Ca Pe^{-1} V^G = -k^G(S) \left(p_X^G + \delta Pe^{-1/2} Bo \right), \tag{5.10b}$$

$$Pe^{-1/2} S_\tau + V_X^L = -\mathcal{A}(S) E(\rho), \tag{5.10c}$$

$$-\delta Pe^{-1/2} S_\tau + V_X^G = \mathcal{A}(S) E(\rho), \tag{5.10d}$$

$$\delta \nu Pe^{-1/2} (1 - S) \rho_\tau + \nu V^G \rho_X = \left(D^{eff}(S) \rho_X \right)_X + (1 - \nu\rho) \mathcal{A}(S) E(\rho). \tag{5.10e}$$

We see that (5.10c)–(5.10e) are all quasi-steady to leading order in $Pe^{-1/2} \ll 1$, with no time derivatives.

Furthermore, since we assume that both $Ca \ll \xi Pe$ and $Ca \ll \sqrt{Pe} \ll Pe$, we see from (5.10a)–(5.10b) that both $p_X^L = 0$ and $p_X^G = 0$ to leading order. Thus, the capillary pressure $p_c(S) = p^G - p^L$ is spatially uniform and so the saturation S is spatially uniform to leading order (although of course it varies with time τ). Since we also found S to be independent of z in the outer region, the saturation is spatially uniform throughout the porous medium and evolves according to the temporal ODE (5.7).

Within the boundary layer, the model reduces at leading order to the ODE system

$$V_X^L = -\mathcal{A}(S) E(\rho), \tag{5.11a}$$

$$V_X^G = \mathcal{A}(S) E(\rho), \tag{5.11b}$$

$$\nu V^G \rho_X = \left(D^{eff}(S) \rho_X \right)_X + (1 - \nu\rho) \mathcal{A}(S) E(\rho), \tag{5.11c}$$

which must be solved at each time τ or, equivalently, for each saturation value $S(\tau)$. We note that (5.11b)–(5.11c) form a closed system for ρ and V^G, upon solution of which V^L is given by (5.11a).

By combining (5.11a)–(5.11b) to obtain an expression of total conservation of mass, we see that $V^L + V^G$ is independent of X and, by both matching with the outer region as $X \to -\infty$ and applying the boundary conditions at $X = 0$, we find that

$$V^L + V^G = V^{L,BL} = V^{G,out}, \tag{5.12}$$

where $V^{G,out}$ is the gas flux out of the top of the porous medium, at $X = 0$ or $z = 1$. The ODE (5.7) for S may therefore equivalently be written as

$$S_\tau = -V^{G,out}. \tag{5.13}$$

Similarly, we note from (5.11b) that the net evaporation rate (4.4) is

$$\text{net evaporation rate} = \int_{z=0}^{1} \mathcal{A}(S) E(\rho) \, \mathrm{d}z = \frac{1}{\sqrt{Pe}} \int_{X=-\infty}^{0} V_X^G \, \mathrm{d}X = \frac{V^{G,out}}{\sqrt{Pe}}. \tag{5.14}$$

To solve (5.11b)–(5.11c) for ρ and V^G (and so find $V^{G,out}$), we must specify a functional form for $E(\rho)$. In the following subsection, we use a linear dependence and find an explicit
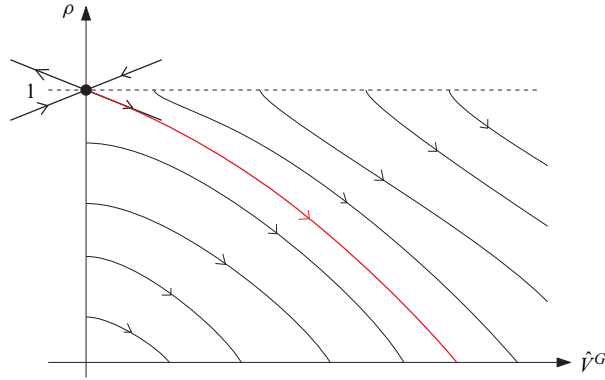
Figure 4. Sketched phase plane portrait for the autonomous system (5.18) in the boundary layer during stage 1. For the required matching with the outer region, the solution trajectory must originate at the critical point $\rho = 1$, $\hat{V}^G = 0$, shown in red.

solution in that case. For general $E(\rho)$, we may combine (5.11b)–(5.11c) to find a first integral

$$V^G(1 - \nu\rho) + D^{eff}\rho_X = 0, \qquad (5.15)$$

where we have fixed the integration constant to be zero by matching with the outer region, in which V^G and ρ_X are both zero. Thus, our third-order problem (5.11b)–(5.11c) reduces to the autonomous, first-order system

$$D^{eff}\rho_X = -(1 - \nu\rho)\, V^G, \qquad V_X^G = \mathcal{A}E(\rho), \qquad (5.16a)$$

with

$$\rho \to 1, \quad V^G \to 0, \qquad \text{as } X \to -\infty. \qquad (5.16b)$$

Furthermore, with the change of variables

$$X = \sqrt{\frac{D^{eff}(S)}{\mathcal{A}(S)}}Y, \qquad V^G = \sqrt{\mathcal{A}(S)D^{eff}(S)}\,\hat{V}^G, \qquad (5.17)$$

the S dependence is removed from (5.16), leaving the system

$$\rho_Y = -(1 - \nu\rho)\,\hat{V}^G, \qquad (5.18a)$$

$$\hat{V}_Y^G = E(\rho), \qquad (5.18b)$$

with

$$\rho \to 1, \quad \hat{V}^G \to 0, \qquad \text{as } Y \to -\infty. \qquad (5.18c)$$

We can understand (5.18) to some extent for generic E with a phase-plane analysis. The phase plane is sketched in figure 4. In particular, the critical point of the system is at $\rho = 1$, $\hat{V}^G = 0$, which we classify as a saddle, so long as $E(\rho)$ is decreasing in ρ at the saturation point $\rho = 1$. Physical solutions must satisfy $\rho \in [0, 1]$ and $\hat{V}^G > 0$. In this range, we see from (5.18a) that ρ is monotone decreasing, while $\hat{V}^G$ is monotone increasing, since $E(\rho) \geqslant 0$. In particular, at $\rho = 0$, we must have ρ_Y non-zero for $\hat{V}^G > 0$, and so we expect solution trajectories to intersect the $\rho = 0$ axis at finite Y and finite $\hat{V}^G > 0$. For the matching conditions (5.18c) as $Y \to -\infty$, the solution trajectory of interest is the unique trajectory that approaches the critical point as $Y \to -\infty$, marked in red in figure 4.

1017 A6-16

Over time, we expect S to decrease. The effective vapour diffusivity D^{eff} is likely to be decreasing in S. The interfacial area fraction $\mathcal{A}$ might have non-montone variation with S, but it is reasonable to assume this is increasing with S, especially as S becomes small. Thus, over time, we might expect variation in the width $\sqrt{D^{eff}/\mathcal{A}}$ of the boundary layer (from (5.17)) and, especially as S begins to become small, we expect the boundary-layer width to increase.

5.1.3. *Solution when E is linear in ρ*

As discussed in §2.2, many models for the evaporation rate E are linear in the vapour density ρ. In this section, we specify the Hertz–Knudsen relation (2.4) so that, in our dimensionless variables,

$$E(\rho) = 1 - \rho. \tag{5.19}$$

With this (commonly used) form for E, we can make analytical progress in solving for boundary-layer processes and, thus, for the evolution of the saturation, S, via (5.13).

With the linear form (5.19), the system (5.18) becomes

$$\rho_Y = -(1 - \nu\rho)\,\hat{V}^G, \tag{5.20a}$$

$$\hat{V}^G_Y = 1 - \rho. \tag{5.20b}$$

Combining these, we find the single, separable equation

$$\frac{\mathrm{d}\rho}{\mathrm{d}\hat{V}^G} = \frac{\rho_Y}{\hat{V}^G_Y} = -\frac{1 - \nu\rho}{1 - \rho}\hat{V}^G, \tag{5.21}$$

with solution

$$\left(\hat{V}^G\right)^2 = \frac{2}{\nu}\left(1 - \rho + \left(\frac{1}{\nu} - 1\right)\log\left(\frac{1 - \nu}{1 - \nu\rho}\right)\right), \tag{5.22}$$

where we have applied the matching conditions with the outer problem to fix the integration constant, specifying that $\rho \to 1$ and $\hat{V}^G \to 0$ as $Y \to -\infty$.

We can now use this relation (5.22) between $\hat{V}^G$ and ρ to find a single, first-order ODE for ρ, by eliminating $\hat{V}^G$ in (5.20a), say. Indeed, doing so results in the implicit solution for ρ

$$\int_{\rho_\infty}^{\rho} \frac{1}{(1 - \nu\tilde{\rho})\sqrt{1 - \tilde{\rho} + (1/\nu - 1)\log\left((1 - \nu)/(1 - \nu\tilde{\rho})\right)}}\,\mathrm{d}\tilde{\rho} = -\sqrt{\frac{2}{\nu}}Y, \tag{5.23}$$

if we impose the boundary condition $\rho = \rho_\infty$ at $Y = 0$.

However, we already gain significant information from this first integral (5.22). Applying the boundary condition for ρ at the top of the porous medium ($z = 1$ or $Y = 0$) in (5.22) gives us precisely the value $V^{G,out} = V^G|_{X=0} = \sqrt{\mathcal{A}D^{eff}}\hat{V}^G|_{Y=0}$ needed to understand the overall evaporation rate $S_\tau = -V^{G,out}$ as in (5.13). We can do this for either choice of boundary condition discussed in §2.3, and now look at each in turn.

Firstly, if we impose the Dirichlet condition for the vapour density $\rho = \rho_\infty$ at the top $Y = 0$, then immediately from (5.22), we see that

$$S_\tau = -V^{G,out} = -\sqrt{\frac{2\mathcal{A}(S)D^{eff}(S)}{\nu}}\sqrt{1 - \rho_\infty + \left(\frac{1}{\nu} - 1\right)\log\left(\frac{1 - \nu}{1 - \nu\rho_\infty}\right)}. \tag{5.24}$$

Although we have worked with ν throughout as an order 1 parameter, it is helpful to note at this point that $\nu = O(10^{-2})$ is actually fairly small. In this case, (5.24) becomes the

simpler expression

$$S_\tau = -V^{G,out} = -\sqrt{\mathcal{A}(S)D^{eff}(S)}\,(1 - \rho_\infty + O(\nu)) \quad \text{if } \nu \ll 1. \tag{5.25}$$

In the case where $\nu \ll 1$, we may also integrate (5.23) to find an explicit solution for ρ and, therefore, $V^G = \sqrt{\mathcal{A}D^{eff}}\hat{V}^G$ via (5.22) in the boundary layer, which is simply $V^G = \sqrt{\mathcal{A}D^{eff}}(1 - \rho) + O(\sqrt{\nu})$ in this limit. We find

$$\rho = 1 - (1 - \rho_\infty)\exp\left(\sqrt{\frac{\mathcal{A}}{D^{eff}}}X\right), \qquad V^G = \sqrt{\mathcal{A}D^{eff}}(1 - \rho_\infty)\exp\left(\sqrt{\frac{\mathcal{A}}{D^{eff}}}X\right), \tag{5.26a}$$

$$V^L = \sqrt{\mathcal{A}D^{eff}}(1 - \rho_\infty)\left(1 - \exp\left(\sqrt{\frac{\mathcal{A}}{D^{eff}}}X\right)\right), \tag{5.26b}$$

where we have used (5.12) to fix V^L and returned to spatial variable $X = \sqrt{(D^{eff}/\mathcal{A})}\,Y$.

We saw in § 5.1.1 that V^L is linear in z in the outer region, while $\rho = 1$ and $V^G = 0$ are constant. We form the leading-order composite solution expansions, valid over the entire domain (outer and boundary layer):

$$\rho = 1 - (1 - \rho_\infty)\exp\left(-\sqrt{\frac{\mathcal{A}Pe}{D^{eff}}}(1 - z)\right), \tag{5.27a}$$

$$U^G = \sqrt{\frac{\mathcal{A}D^{eff}}{Pe}}(1 - \rho_\infty)\exp\left(-\sqrt{\frac{\mathcal{A}Pe}{D^{eff}}}(1 - z)\right), \tag{5.27b}$$

$$U^L = \sqrt{\frac{\mathcal{A}D^{eff}}{Pe}}(1 - \rho_\infty)\left(z - \exp\left(-\sqrt{\frac{\mathcal{A}Pe}{D^{eff}}}(1 - z)\right)\right). \tag{5.27c}$$

This completes our analysis of stage-1 drying with the Dirichlet boundary condition; we will consider the flux condition shortly. First, however, we note from (5.24) that if the product $\mathcal{A}(S)D^{eff}(S)$ is constant (independent of S), then the net evaporation rate is constant, as expected in this 'constant rate period' of the drying. Various experimental measurements show that the net evaporation rate is usually not strictly constant during stage 1, but could either rise or fall (Wu & Prat 2022). We would expect $D^{eff}(S)$ to be a decreasing function of S: with less liquid in the pore space, the effective rate of the diffusion of vapour is increased. The dependence of the liquid–gas surface area $\mathcal{A}(S)$ will depend heavily on the pore geometry, but we might expect that $\mathcal{A}$ is an increasing function of S, at least for fairly small S. Our analysis suggests that it is the interplay between these effects that determine whether the evaporation rate, given by (5.24) and proportional to $\sqrt{\mathcal{A}D^{eff}}$, rises or falls over stage 1.

In figure 5, we show the time variation of the net evaporation rate for three different pairs of $\mathcal{A}$ and D^{eff}, showing a rising, falling and truly constant rate. The drying rate during stage 1 is very well predicted by (5.24) (dashed green curves) for all cases. The time at which stage 1 ends is not very well captured by (5.24), although this improves for larger Pe and smaller Ca (this is discussed further in § 5.2).

In figure 5(*b–d*), we compare the numerically computed profiles of S, ρ, U^L and U^G against the solution of the asymptotic reduction (5.24) and the corresponding composites (5.27). We take $\mathcal{A}$ and D^{eff} constant, so that the approximate ρ, U^L and U^G profiles (5.27) are independent of S, and so of time. The vapour density ρ and gas velocity U^G are very
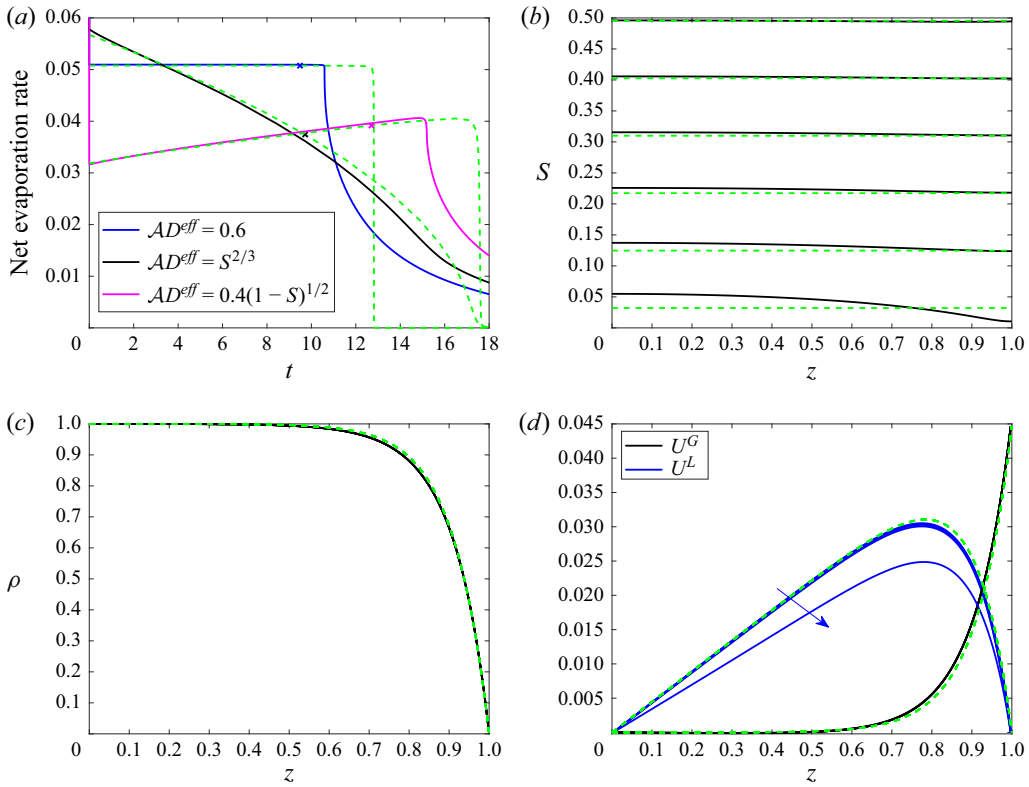
Figure 5. Stage-1 drying. Numerical solutions (solid curves) of (3.3) compared with the large-Pe approximation (dashed green) where S is the solution of the ODE (5.24), and the analytical expressions for ρ, U^L and U^G are (5.27). (*a*) Comparison of numerical (solid colour) and asymptotic (green dashed) net evaporation rates (4.4) for various $\mathcal{A}$ and D^{eff} (with $Ca = 1$). Crosses mark the point where S computed from (5.24) reaches $Ca Pe^{-1/2}$. (*b–d*) Numerical and approximate profiles of S, ρ, U^L and U^G at uniform time steps through stage 1, with $\mathcal{A} = 0.5$, $D^{eff} = 1$ constant (with $Ca = 0.1$). In panel (*d*), the arrow shows direction of increasing time for the numerical U^L profile. Throughout, we take $Pe = 250$, $\nu = 0.2$, $\xi = 0.5$ and all other parameters as in table 2.

well approximated by (5.27), as are S and U^L for the majority of stage 1. However, as the saturation S becomes smaller, it is no longer spatially uniform and the liquid flux U^L is reduced. This is due to the viscous drag force, neglected in our stage-1 approximation, becoming important and hindering the capillary flow. We discuss this further in § 5.2.

The above mentioned analysis is for the case of a Dirichlet boundary condition for ρ at the surface. In the alternative case, the boundary condition for ρ at the surface of the porous medium is the Newton-cooling mass flux condition

$$\nu U^G \rho - Pe^{-1} D^{eff} \rho_z = m(\rho - \rho_\infty) \qquad \text{at } z = 1. \qquad (5.28)$$

In our boundary-layer variables, this becomes

$$\nu V^G \rho - D^{eff} \rho_X = M(\rho - \rho_\infty) \qquad \text{at } X = 0, \qquad (5.29)$$

where $M = m\sqrt{Pe}$. If $M \gg 1$, then we regain the Dirichlet condition $\rho = \rho_\infty$. The case where $M \ll 1$ corresponds to vapour transport through the air being much slower than vapour diffusion through the porous medium, and thus mass transfer external to the material directly sets the evaporation rate (we do not consider this case further here). If $M = O(1)$, then we note from the first integral (5.15) that this boundary condition (5.29)
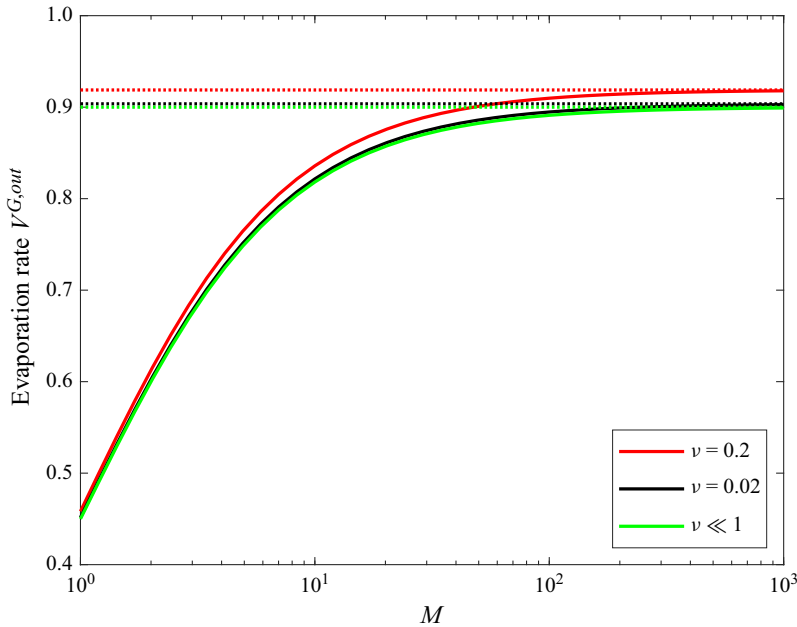
Figure 6. Net evaporation rate $V^{G,out}$ during stage 1 as a function of the mass-transfer rate through the surrounding air, M. Solid curves are the solution of (5.31) and dotted curves are in the large-M limit where we regain (5.24), the case of a Dirichlet boundary condition. We use $\rho = 0.1$, $\mathcal{A}D^{eff} = 1$.

may be written as

$$V^G = M(\rho - \rho_\infty) \qquad \text{at } X = 0. \tag{5.30}$$

Evaluating (5.22) at $X = Y = 0$ and applying (5.30), we obtain an algebraic equation satisfied by $V^{G,out} = \sqrt{\mathcal{A}D^{eff}} \hat{V}^G|_{Y=0}$, namely

$$\frac{(V^{G,out})^2}{2\mathcal{A}D^{eff}} = \frac{1}{\nu} \left(1 - \rho_\infty - \frac{V^{G,out}}{M} + \left(\frac{1}{\nu} - 1 \right) \log \left(\frac{1 - \nu}{1 - \nu\rho_\infty - \nu V^{G,out}/M} \right) \right). \tag{5.31}$$

In the case where $\nu \ll 1$, we can solve for the leading-order $V^{G,out}$, finding that

$$V^{G,out} = \sqrt{\mathcal{A}D^{eff}} \left(\frac{1 - \rho_\infty}{1 + \sqrt{\mathcal{A}D^{eff}/M}} \right) + O(\nu) \qquad \text{if } \nu \ll 1. \tag{5.32}$$

As in the case of the Dirichlet boundary condition, the solution $V^{G,out}(S)$ of (5.31) then gives the net rate of evaporation, according to (5.14). We plot solutions $V^{G,out}$ of (5.31) in figure 6 and, in particular, see that for the physical value $\nu = 0.02$, there is excellent agreement with the $\nu \ll 1$ approximation (5.32).

5.2. *Transition from stage 1 to stage 2*

Consistent with experimental and numerical results in the literature (e.g. Pel *et al.* 1996), all our numerical simulations of the full model (3.3) shown so far exhibit a sudden end to stage 1 and a rapid transition to stage 2 (analysed in § 5.3). Stage 1 is generally understood to end when the capillary forces are no longer sufficiently strong relative to the viscous drag to draw liquid to the surface of the porous medium. We saw in figure 2 that the transition occurs when first $S = 0$ at $z = 1$. In the literature, the transition is observed to

occur when the average saturation dips below a critical value (Gupta *et al.* 2014; Hall & Hoff 2021), often seen to be around 0.1–0.3, but strongly dependent on the properties of the porous medium and varying with the evaporation rate (Gupta *et al.* 2014).

From our asymptotic analysis, we are in a position to quantify the scaling for this critical saturation, and its dependence on the system parameters and constitutive laws. We note that the reduced model for stage 1 given in § 5.1 does not directly capture the transition, as the solution S is spatially uniform. However, we see that our reduced stage-1 model must break down if $k^L(S)p_c(S)$ approaches zero. Specifically, if at some saturation S we have a small $k^L(S)p_c(S) = O(CaPe^{-1/2}) \ll 1$, then the viscous drag becomes large enough to balance the capillary forces in (3.3a). Capillary forces then no longer dominate over the order-one domain and so we no longer expect a uniform saturation profile through the porous medium. This slowing of the liquid flux by viscous drag is what eventually leads to a zero liquid saturation at the surface. The balance of capillary and viscous forces in (3.3a), with the stage-1 scaling $U^L = O(Pe^{-1/2})$, gives an estimate for the critical saturation: viscous forces will become non-negligible, heralding the end of stage 1, when $S = O(S_{crit})$ defined by

$$k^L(S_{crit})p_c(S_{crit}) = CaPe^{-1/2}. \tag{5.33}$$

If, for instance, $k^L(S)p_c(S) \sim S^n$ as $S \to 0$ for some $n > 0$, then the critical saturation is estimated as $S_{crit} \approx Ca^{1/n}Pe^{-1/(2n)}$. Furthermore, a lower bound on the transition time between stage 1 and stage 2, t_*, is given by the time at which the (spatially uniform) solution of the reduced model (5.24) satisfies $k^L(S)p_c(S) = CaPe^{-1/2}$, or $S = S^{crit}$. By integrating (5.24), we find this (under) estimate for the transition time t_* to be

$$t_*^{lower} = \sqrt{Pe}\sqrt{\frac{\nu}{2\left(1 - \rho_\infty + \left(\frac{1}{\nu} - 1\right)\log\left(\frac{1-\nu}{1-\nu\rho_\infty}\right)\right)}} \int_{S_{crit}}^{S_0} \frac{1}{\sqrt{\mathcal{A}(S)D^{eff}(S)}}\,\mathrm{d}S. \tag{5.34a}$$

This lower bound (5.34a) on t_* is marked with a cross in figure 5(a), for each of the different functional forms for $\mathcal{A}(S)$ and $D^{eff}(S)$.

Conversely, as observed in figure 5(a), allowing our stage-1 reduced model (5.24) to run until $S = 0$ may be used to find an upper bound on the time t_* of the transition to stage 2. Specifically, by integrating (5.24), this upper bound is

$$t_*^{upper} = \sqrt{Pe}\sqrt{\frac{\nu}{2\left(1 - \rho_\infty + \left(\frac{1}{\nu} - 1\right)\log\left(\frac{1-\nu}{1-\nu\rho_\infty}\right)\right)}} \int_0^{S_0} \frac{1}{\sqrt{\mathcal{A}(S)D^{eff}(S)}}\,\mathrm{d}S. \tag{5.34b}$$

The true transition time found in the full numerical solution appears to lie fairly centrally in the interval $[t_*^{lower}, t_*^{upper}]$ for each case shown in figure 5.

Physically, we expect $k^L(S)$ to become small for sufficiently small S, while we expect that p_c should grow as S becomes small. It is very interesting that we require the product $k^L(S)p_c(S)$ to become small for stage 1 to end, as this is not true in general: for instance, if we choose $k^L = S$ and $p_c \sim 1/S$ as $S \to 0$, which seem to have the correct behaviour described in § 2.2, then the product $k^L p_c \to 1$ as $S \to 0$. As shown in figure 7, there is no stage 2 in this drying scenario: S remains uniform at all times and stage 1 lasts until the drying is complete, so that our stage-1 reduced model (5.24) remains valid for the entire drying process. Similar behaviour to this was seen experimentally by Gupta *et al.* (2014). They observed that the crystallisation of salt within the pore space of building
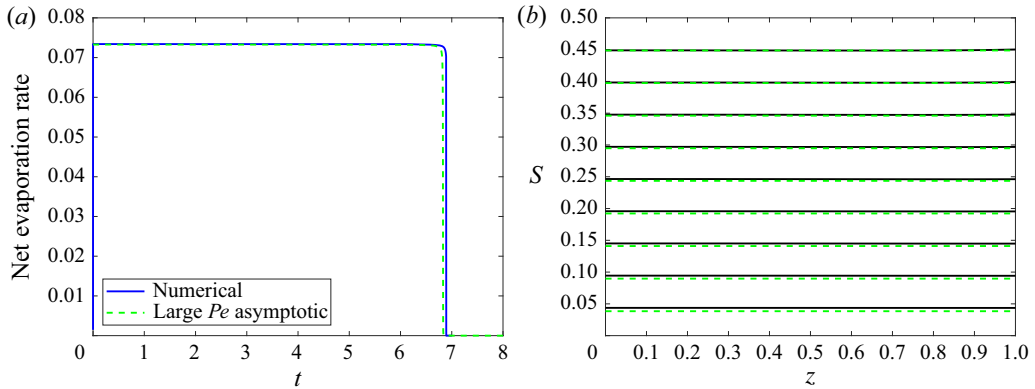
Figure 7. Drying with no stage 2 when $k^L(S) = S$, $p_c(S) = 1/S - S$, so that $k^L p_c \sim 1$ as $S \to 0$. Numerical solutions of the full model (3.3) (solid curves) compared with the stage-1 model (5.24) (green dashed). Here, we take $\mathcal{A} = 0.5$ and $D^{eff} = 1$ constant, $Pe = 100$, $Ca = 0.1$, and all other parameters as in table 2.

materials during drying impeded the onset of stage 2, so that constant-rate-period drying, with uniform saturation profiles, was seen to last throughout the entire drying process. Using a simplified continuum model, Gupta *et al.* (2014) gave a qualitatively similar (although less general) method to compute the critical saturation. In light of our analysis, we might interpret the results of Gupta *et al.* (2014) to mean that the presence of salt crystals increased the permeability and/or capillary pressure of the material to the extent that $k^L p_c$ did not become sufficiently small to trigger stage 2.

Since the qualitative drying behaviour (the existence of a stage 2) depends on the behaviour of these constitutive laws $k^L(S)$ and $p_c(S)$ for small S, it is critical that these are chosen appropriately for the porous medium and drying scenario at hand, if we hope to capture the real drying behaviour.

5.3. *Stage 2: the 'receding front period'*

We now consider the behaviour during stage 2 of the drying, for $t > t_*$, when we expect the evaporation rate to drop and a drying front to recede into the porous medium.

We look for a receding drying front at $z = h(t)$, with a wet region ($S > 0$) for $0 < z < h$ and a dry region ($S = 0$) for $h < z < 1$. A schematic diagram for stage 2 is shown in figure 8. Since $Pe \gg 1$, following the same argument as in § 5.1 for stage 1, the evaporation term dominates the vapour density equation (3.3e) in the wet region $z < h$, so that $\rho = 1$ with exponentially small error in that region. We therefore expect that the evaporation will take place only in a thin transition layer at the front $z = h$. Throughout this section, we take the local evaporation rate $E(\rho) = 1 - \rho$ to be linear in ρ.

During stage 2, the saturation S is small, since, as we have seen in § 5.2, the viscous drag must be too strong for the capillary forces to pull liquid fully to the surface of the porous medium (so that stage-1 drying stops). We will actually find that it is appropriate to take different scalings for S in the wet region $z < h$ and in the transition layer near to $z = h$. We use the saturation scalings

$$S = \eta \hat{S}, \quad \text{in } z < h, \qquad S = \bar{\eta} \bar{S}, \quad \text{in the transition layer,} \qquad (5.35)$$

where $\bar{\eta} \ll \eta \ll 1$ which we specify later. We suppose that $\mathcal{A} \sim S^m$ and $k^L p_c \sim S^n$ as $S \to 0$ (with both powers $n, m > 0$). Given this behaviour, we see that in the transition layer,
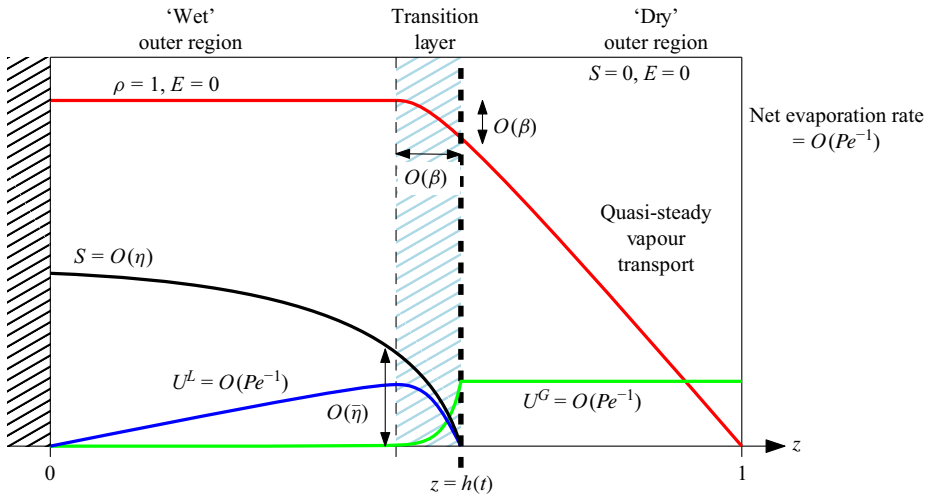
Figure 8. Schematic diagram showing the solution structure during stage 2, with a receding drying front at $z = h(t)$.

$$\mathcal{A}(S) = \bar{\eta}^m \bar{\mathcal{A}}(\bar{S}), \qquad k^L(S) p_c(S) = \bar{\eta}^n \bar{k}^L(\bar{S}) \bar{p}_c(\bar{S}), \tag{5.36}$$

while in the wet region, $z < h$,

$$k^L(S) p_c(S) = \eta^n \hat{k}^L(\hat{S}) \hat{p}_c(\hat{S}). \tag{5.37}$$

We will assume in the subsequent analysis that $n > m$, so that the capillary flow rate $k^L p_c$ approaches zero at a faster rate as the saturation decreases than the liquid–gas interfacial area $\mathcal{A}$.

To investigate the moving front behaviour, we rescale into a thin transition layer at $z = h$, by making the change of variables

$$t = t_* + \eta Pe T, \qquad z = h(T) + \beta X, \qquad \rho = 1 - \beta \bar{\rho}, \qquad E = \beta \bar{\rho}, \tag{5.38a}$$

$$U^G = \frac{1}{Pe} W^G, \qquad U^L = \frac{1}{Pe} W^L, \qquad p^G = \tilde{p}^G(h) + \frac{Ca\beta}{Pe\xi} \bar{p}^G. \tag{5.38b}$$

Here, the thickness of the transition layer is

$$\beta = \bar{\eta}^{-m/2} Pe^{-1/2} \ll 1, \tag{5.39}$$

so that there is a balance of evaporation in the transition layer and (largely diffusive) transport of vapour out of the porous medium through the dry region. If $m > 0$, this transition layer is wider than the $O(Pe^{-1/2})$ boundary layer during stage 1, since $\bar{\eta} \ll 1$. The variation of the vapour density from its saturation value 1, in (5.38), must be of order β in the transition layer to match the vapour flux leaving the transition layer with that through dry outer region $z \in (h, 1)$. A balance in the liquid Darcy's law (3.3a) in the transition layer requires that

$$\bar{\eta}^n = \frac{\beta Ca}{Pe}. \tag{5.40}$$

The two constraints (5.39) and (5.40) fix the transition-layer width and saturation scaling to be

$$\beta = Ca^{-\frac{m}{m+2n}} Pe^{-\frac{(n-m)}{m+2n}}, \qquad \bar{\eta} = Ca^{\frac{2}{m+2n}} Pe^{-\frac{3}{m+2n}} \tag{5.41}$$

1017 A6-23

although we will retain the β and $\bar{\eta}$ notation for simplicity. In particular, since $Pe \gg 1$, we have $\bar{\eta} \ll 1$ and the transition-layer thickness β is small so long as $m < n$, which we require to be the case for the transition-layer structure to be valid.

The time scale stated in (5.38) of the stage-2 drying is ηPe, which is determined by a balance in the liquid mass conservation equation (3.3c) in the wet region. The velocity scales in (5.38) (which we note are smaller than stage 1) are determined by the liquid and gas mass equations, and the gas pressure scale comes from the gas Darcy law (3.3b) (with $\tilde{p}^G(h)$ independent of X and set by the gas transport in the outer region, as we will see later). We note that with these scalings, the net evaporation rate (4.4) is

$$\text{net evaporation rate} = Pe^{-1} \int_{X \to -\infty}^{\infty} \hat{\mathcal{A}} \hat{\rho} \, \mathrm{d}X, \tag{5.42}$$

of order Pe^{-1}, and so slower than during stage 1 (where the net evaporation rate was $O(Pe^{-1/2})$), as we expect.

Since the liquid velocity scale in the wet region $z < h$ must be the same as that in the transition layer (i.e. of order Pe^{-1}), a distinguished limit of the model is when the viscous and capillary forces in Darcy's law balance in the wet region, so that the saturation scaling here is given by

$$\eta = \left(\frac{Ca}{Pe} \right)^{1/n}. \tag{5.43}$$

At the end of stage 1, we saw in § 5.2 that the saturation scaled with $Ca^{1/n}Pe^{-1/2n}$, which is larger than η defined in (5.43). Thus, we might actually expect saturations larger than $O(\eta)$ (defined in (5.43)) at the start of stage 2. However, we will see that the large-$\hat{S}$ case is contained within the distinguished limit and thus may use the distinguished-limit saturation scaling (5.43) for stage 2. We also note that $\bar{\eta} = \beta^{1/n}\eta$, so that the transition-layer saturation is smaller than the wet-region saturation, as expected.

With these changes of variable (5.38), we find that to leading order in the transition layer, the model (3.3) becomes

$$W^L = \bar{k}^L \bar{p}_{cX}, \tag{5.44a}$$

$$W^G = -k^G \bar{p}_X^G, \tag{5.44b}$$

$$W_X^L = -\bar{\mathcal{A}} \bar{\rho}, \tag{5.44c}$$

$$W_X^G = \bar{\mathcal{A}} \bar{\rho}, \tag{5.44d}$$

$$0 = -\left(D_0^{eff} \bar{\rho}_X \right)_X + (1 - \nu) \bar{\mathcal{A}} \bar{\rho}, \tag{5.44e}$$

where $D_0^{eff} = D^{eff}(0)$. These transition-layer equations (5.44) are closed by matching with the surrounding $O(1)$-length scale regions.

With the same time and velocity scales, and scaling $p^G = CaPe^{-1}\xi^{-1}\tilde{p}^G$, we see that to leading order in the dry region $h(T) < z < 1$,

$$W_z^G = 0, \qquad W^G = -\tilde{p}_z^G, \qquad \nu W^G \rho_z = D_0^{eff} \rho_{zz}. \tag{5.45}$$

At the surface $z = 1$, we impose the Dirichlet condition $\rho = \rho_\infty$, noting that, at the slower evaporation rates during stage 2 than in stage 1, we expect that the alternative mass flux condition (3.5c) (left) reduces to this Dirichlet form at leading order.

In the wet region $0 < z < h(T)$, since $E = 0$, we must have no gas flow $W^G = 0$ and constant gas pressure $p^G = \tilde{p}^G(h)$. The liquid equations are

$$\hat{S}_T + W_z^L = 0, \qquad W^L = \hat{k}^L \hat{p}_{cz}, \tag{5.46}$$

which combine to a single diffusion equation for S, namely

$$\hat{S}_T + \left(\hat{k}^L(\hat{S}) \hat{p}_c'(\hat{S}) \hat{S}_z\right)_z = 0. \tag{5.47}$$

5.3.1. *Gas and vapour flow*

We first study the gas and vapour flow through the dry region $h < z < 1$ and the transition layer. In this dry region, from (5.45), we see that $W^G = W_{dry}^G(T)$ is spatially uniform. By combining the transition-layer equations (5.44d)–(5.44e), we see that the quantity

$$(1 - v)W^G - D_0^{eff} \bar{\rho}_X = 0 \tag{5.48}$$

is conserved over the transition layer, and equal to zero by matching with the wet region $z < h$ where there is no gas flow or vapour flux. Matching also with the dry region $z > h$, we find that

$$(1 - v)W_{dry}^G = D_0^{eff} \bar{\rho}_X \Big|_{X=0} = -D_0^{eff} \rho_z \Big|_{z=h}. \tag{5.49}$$

Solving the vapour equation (5.45) (right) subject to the matching conditions (5.49) and $\rho = 1$ at $z = h$, and the boundary condition $\rho = \rho_\infty$ at $z = 1$, we obtain the solution in the dry region $z \in (h, 1)$:

$$\rho = \frac{1}{v}\left(1 - (1 - v\rho_\infty)\left(\frac{1 - v}{1 - v\rho_\infty}\right)^{\frac{1-z}{1-h}}\right), \qquad W_{dry}^G = \frac{D_0^{eff} \log\left(\frac{1 - v\rho_\infty}{1 - v}\right)}{v(1 - h)}. \tag{5.50a}$$

Then, solving (5.45) (centre), with $\tilde{p}^G = 0$ at the surface $z = 1$, we see that the gas pressure through the dry region is

$$\tilde{p}^G = W_{dry}^G(1 - z). \tag{5.50b}$$

The constant gas pressure in the wet region is therefore

$$\tilde{p}^G(h) = W_{dry}^G(1 - h) = \frac{D_0^{eff} \log\left(\frac{1 - v\rho_\infty}{1 - v}\right)}{v}, \tag{5.51}$$

independent of both space and time (as observed numerically in figure 2d). As an aside, for small $v \ll 1$, we note that (5.50) reduce to

$$\rho = \rho_\infty + (1 - \rho_\infty)\frac{1 - z}{1 - h} + O(v), \qquad W_{dry}^G = \frac{D_0^{eff}}{1 - h}(1 - \rho_\infty) + O(v) \qquad \text{as } v \to 0. \tag{5.52}$$

We have thus found the vapour and gas solutions in the order-1 wet and dry regions, in terms of the (as yet unknown) position, h, of the drying front. Additionally, by integrating the transition-layer equation (5.44d) over the entire transition layer and matching with the behaviour in the wet and dry regions on either side, we see that the net evaporation rate (5.42) over the transition layer – and so over the entire material since the transition layer

is the only region with non-negligible evaporation – is

$$\text{(net evaporation rate) } Pe = \int_{X \to -\infty}^{\infty} \hat{\mathcal{A}}\hat{\rho}\, \mathrm{d}X = W_{dry}^G = \frac{D_0^{eff} \log\left(\frac{1 - \nu\rho_\infty}{1 - \nu}\right)}{\nu(1 - h)}. \quad (5.53)$$

Thus, given the position $h(T)$ of the receding front, the vapour transport through the dry region determines the net evaporation rate. However, $h(T)$ is still to be determined: to understand how the receding front moves, we must consider the liquid problem in the wet region and transition layer.

5.3.2. *Liquid flow and the receding front*

In the wet region $z \in (0, h(T))$, the saturation $\hat{S}$ satisfies (5.47), with $W^L = \hat{k}^L \hat{p}_{cz} = 0$ at $z = 0$, while in the transition layer, combining (5.44*a*) and (5.44*c*), we find

$$\left(\bar{k}^L(\bar{S})\bar{p}_c'(\bar{S})\bar{S}_X\right)_X = -\bar{\mathcal{A}}\bar{\rho}, \quad (5.54)$$

with $\bar{S} \to 0$ and $W^L = \bar{k}^L \bar{p}_{cX} \to 0$ as $X \to \infty$. The matching conditions between the wet and transition-layer regions are

$$\lim_{z \to h}(\hat{S}) = 0 \quad \text{and} \quad \lim_{z \to h}\left(\hat{k}^L \hat{p}_c' \hat{S}_z\right) = \lim_{X \to -\infty}\left(\bar{k}^L \bar{p}_c' \bar{S}_X\right), \quad (5.55)$$

equivalent to imposing continuity of saturation and liquid flux W^L.

Integrating (5.54) in X over the entire transition layer, using (5.53) and the fact that $\bar{S} \to 0$ and $W^L \to 0$ as $X \to \infty$, we find that

$$W_{dry}^G = \int_{X \to -\infty}^{\infty} \bar{\mathcal{A}}\bar{\rho}\, \mathrm{d}X = \left.\left(\bar{k}^L(\bar{S})\bar{p}_c'(\bar{S})\bar{S}_X\right)\right|_{X \to -\infty}. \quad (5.56)$$

Matching with the wet region using (5.55) (right), this gives

$$\left.\left(\hat{k}^L(\hat{S})\hat{p}_c'(\hat{S})\hat{S}_z\right)\right|_{z=h} = W_{dry}^G, \quad (5.57)$$

which we can view as a boundary condition on the problem (5.47) in the wet region.

Using the expression (5.50*a*) for W^G, we therefore obtain a free-boundary problem on the wet region, namely

$$\hat{S}_T + \left(\hat{k}^L \hat{p}_c' \hat{S}_z\right)_z = 0 \qquad \text{for } 0 < z < h(T), \quad (5.58a)$$

$$\hat{S}_z = 0 \qquad \text{on } z = 0, \quad (5.58b)$$

$$\hat{k}^L \hat{p}_c' \hat{S}_z = \frac{D_0^{eff} \log\left(\frac{1 - \nu\rho_\infty}{1 - \nu}\right)}{\nu(1 - h)} \qquad \text{on } z = h(T), \quad (5.58c)$$

$$\hat{S} = 0 \qquad \text{on } z = h(T). \quad (5.58d)$$

This system (5.58) is a closed problem for $\hat{S}(z, T)$ and $h(T)$. We note that $\hat{S} \to 0$ and so $\hat{k}^L \hat{p}_c' \to 0$ as $z \to h$. The flux remains bounded, but the gradient $\hat{S}_z$ must blow up here. The initialisation of the system (5.58) is not trivial, since the flux in (5.58*c*) blows up as $h \to 1$. We note that if h is close to 1 and $\hat{S}$ is large, then the capillary flow term $\hat{k}^L \hat{p}_c' \hat{S}_z$ dominates and liquid may easily be drawn to the evaporation front at the rate given by (5.58*c*). In practice, we may therefore initialise (5.58) at some h close to 1 and with a large $\hat{S}$: over a fast initial transient, $\hat{S}$ reduces to be of order 1 and $h(T)$ will not

begin to vary appreciably until this point. Thus, the system (5.58) is independent of the initialisation, up to the translation in time to account for the initial transient.

Given the solution of (5.58), we have the saturation, fluid velocity and pressure, and vapour density profiles throughout the order-1 length scale wet and dry regions, as well as the evolution of the receding drying front $h(T)$ and the net drying rate via (5.53).

Similarly to our analysis in stage 1, by integrating over the thin evaporating layer (here the transition layer moving with the receding front, rather than the stationary boundary layer at the surface as in stage 1), we have derived a reduced problem which gives the leading-order evaporation rate. We note that the dependence of the flux boundary condition (5.58c) on $1 - h$ precludes the possibility of a similarity solution and, therefore, expect that the reduced model (5.58) must be solved numerically. We will find numerical solutions for an example form of $\hat{k}^L \hat{p}_c$ in § 5.3.3.

Given the solution of (5.58) and thus the leading-order drying behaviour, we might then solve the transition-layer problem (5.44) to find the behaviour within the transition layer. We note that several of the equations (5.44) decouple, so that we need only solve the coupled diffusion equations for $\bar{S}$ and $\bar{\rho}$, namely

$$\left(\bar{k}^L \bar{p}_c' \bar{S}_X\right)_X = -\bar{\mathcal{A}}(\bar{S})\bar{\rho}, \tag{5.59a}$$

$$D_0^{eff} \bar{\rho}_{XX} = (1 - \nu)\bar{\mathcal{A}}(\bar{S})\bar{\rho}, \tag{5.59b}$$

closed by matching to the leading-order solution on either side as $X \to \pm\infty$. Given the solution of this transition-layer problem (5.59), we may then straightforwardly compute W^L, W^G and $\bar{p}^G$ in the transition layer from (5.44). The solution of this transition-layer problem (5.59) will also motivate an $O(\beta)$ correction to the position h of the receding front. We explore this for the example drying scenario in § 5.3.3.

In this section, we have derived a reduced model describing the motion of a drying front into the porous medium during stage-2 drying, in the case of $Pe \gg 1$. The model is valid so long as $\hat{S}$ remains of order 1. It breaks if the wet-region saturation $\hat{S} = O(\beta^{1/n})$ shrinks to the same size as the saturation ($\bar{S}$, remaining order 1) in the transition layer. The model also ceases to be valid when the receding front h approaches within an $O(\beta)$ length scale of the end of the domain at $z = 0$.

5.3.3. *Example and comparison with numerical solution*

To illustrate the analysis of the previous section, we consider the example constitutive laws

$$k^L(S) = S^3, \qquad p_c(S) = \frac{1}{S} - S, \qquad \mathcal{A} = \begin{cases} \text{constant} & \text{for } S > 0, \\ 0 & \text{for } S = 0. \end{cases} \tag{5.60}$$

Thus, for this example, we have $m = 0$ and $n = 2$, so that

$$\beta = Pe^{-1/2}, \qquad \bar{\eta} = Ca^{1/2}Pe^{-3/4}, \qquad \eta = Ca^{1/2}Pe^{-1/2}. \tag{5.61}$$

From (5.60), we have $k^L p_c' = -S - S^3 \approx -S$ since S is small. The wet-region reduced model (5.58) is therefore

$$\hat{S}_T - \left(\hat{S}\hat{S}_z\right)_z = 0 \qquad \text{for } 0 < z < h(T), \tag{5.62a}$$

$$\hat{S}_z = 0 \qquad \text{on } z = 0, \tag{5.62b}$$

$$-\hat{S}\hat{S}_z = \frac{D_0^{eff} \log\left(\dfrac{1 - \nu\rho_\infty}{1 - \nu}\right)}{\nu(1 - h)} \qquad \text{on } z = h(T), \tag{5.62c}$$

$$\hat{S} = 0, \qquad \text{on } z = h(T). \tag{5.62d}$$

To solve (5.62) numerically for $\hat{S}$ and h, we make a change of variables $z = h(T)y$ so that the model (5.62) holds on the fixed domain $y \in (0, 1)$. We discretise using the method of lines, upwinding the spatial derivatives in the artificial advection terms introduced by the change of variables and with central differences otherwise. The discretised system is solved in MATLAB using the same solver ode15s as for the full system. As discussed for (5.58), the reduced model (5.62) is difficult to initialise numerically since (5.62c) becomes unbounded as $h \to 1$. We initialised close to $h = 1$, but found that up to a shift in T, the solution obtained was independent of the choice of initialisation.

A solution computed in this way is shown in figure 9 (dashed magenta lines) and compared with solutions of the full model (3.3) (solid lines). We find excellent agreement up to the expected error, the width of the transition layer, which is of order $\beta = Pe^{-1/2} \approx 0.03$ in this example. From figure 9(a), we see that the shapes of the $S(z)$ profiles are well captured through the wet region, until we reach the transition region where S approaches zero. Since the reduced model (5.62) prescribes $S = 0$ at the edge of the wet region, the position, h, of the drying front is therefore under-predicted, as seen in figure 9(b), although still within the expected $O(\beta)$ error. Although the position, h, is under-predicted by the reduced model, the net evaporation rate in figure 9(d) is captured very precisely (except for the very start and end of stage 2, when we do not expect our reduced model to be valid).

From figure 9(b), we observe (for both the full numerical solution and the reduced model solution) that the drying front velocity increases over time. This is because the saturation S decreases over time, meaning both that the capillary flow rate decreases (so less liquid can be transported to the drying front) and also that there is simply less liquid at the front to vaporise. To meet the required vaporisation flux, W_{dry}^G, (which depends only on h, not on S), the front must move faster. We emphasise that this increasing-speed drying front is contrary to the decreasing $t^{-1/2}$ front velocity we would find if there was no liquid capillary flow and the front motion was purely determined by the diffusion of vapour out of the material (as in e.g. Luckins *et al.* 2023).

The liquid flux $W^L = -\hat{S}\hat{S}_z$ in the wet region captures the magnitude and gradient of the numerical velocity field well in figure 9(c), until the transition layer is reached. Similarly in figures 9(e)– 9(f), we see that the dry-region vapour density ρ and gas-flux W^G are well captured by (5.50a), up to the expected $O(\beta)$ error.

Due to the simple, piecewise-constant form (5.60) of $\mathcal{A}$ in this example, we may easily solve the transition-layer equation (5.59b) for $\bar{\rho}$ to find

$$\bar{\rho} = W_{dry}^G \sqrt{\frac{1-\nu}{\bar{\mathcal{A}} D_0^{eff}}} \exp\left(\sqrt{\frac{\bar{\mathcal{A}}(1-\nu)}{D_0^{eff}}} X\right) \quad \text{for} \quad X \leqslant 0, \tag{5.63}$$

having used the matching conditions $\bar{\rho} \to 0$ as $X \to -\infty$ and (5.49) at $X = 0$, and where $W_{dry}^G(h(T))$ is given by (5.50a). From (5.44c) and (5.44d), we then find that the Darcy velocities in the transition layer are, for $X \leqslant 0$,

$$W^G = W_{dry}^G \exp\left(\sqrt{\frac{\bar{\mathcal{A}}(1-\nu)}{D_0^{eff}}} X\right), \qquad W^L = W_{dry}^G \left(1 - \exp\left(\sqrt{\frac{\bar{\mathcal{A}}(1-\nu)}{D_0^{eff}}} X\right)\right), \tag{5.64}$$

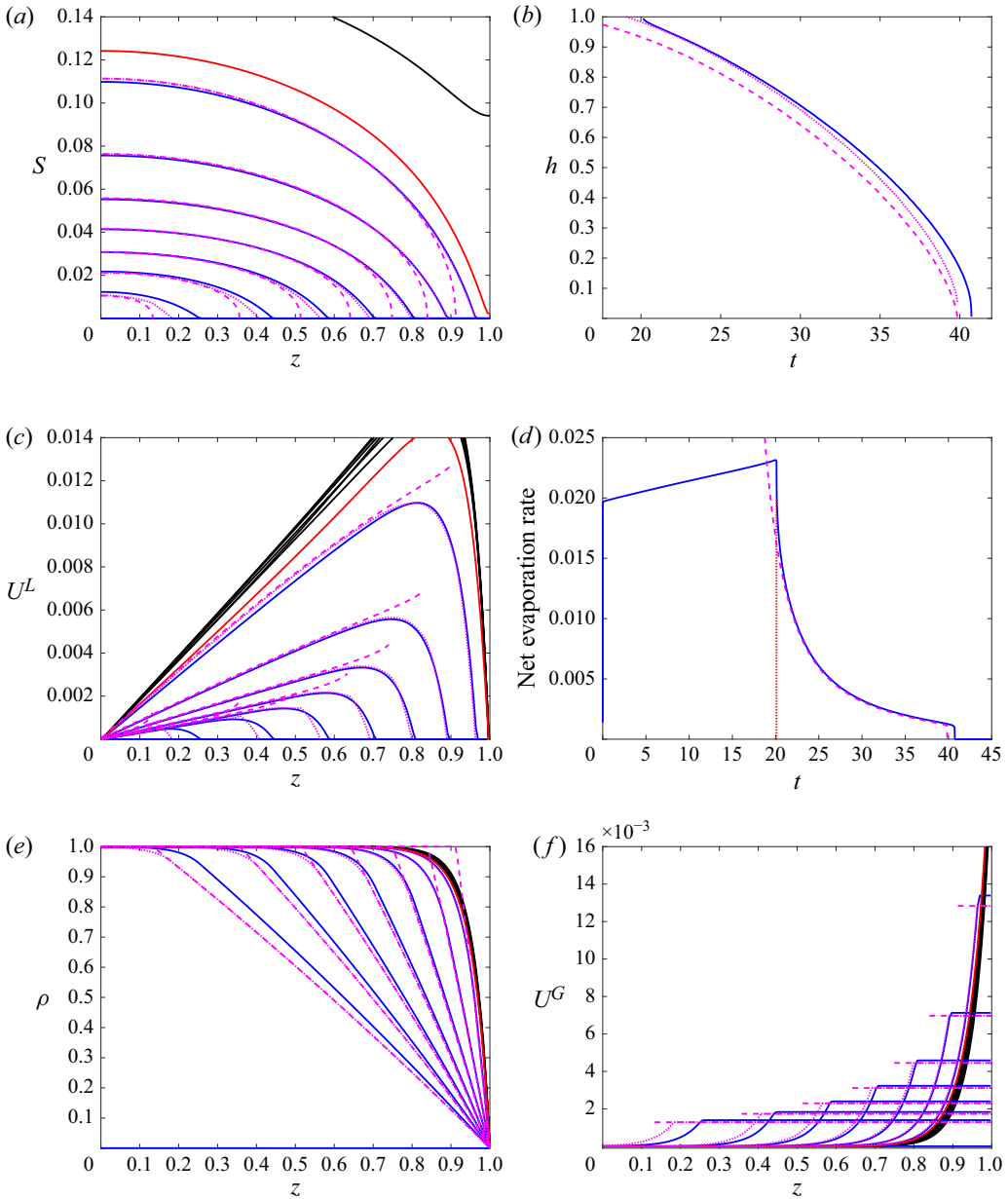and by integrating (5.59a) and imposing that $\bar{S} = 0$ at $X = 0$, we find the saturation is

Figure 9. Stage-2 drying. Numerical solutions of (3.3) (solid curves, colour indicates stage 1 versus stage 2, with parameters as in figure 2), are compared with the solutions of the leading-order Stage-2 reduced model (5.58) (magenta dashed curves). (*a–b*) Direct solutions S and h of (5.58); (*c*) liquid velocity, U^L, for the wet region; (*d–f*) the evaporation rate, (5.53), the dry-region vapour density, and gas velocity (5.50), all computed using the solution h from panel (*b*). We additionally show the composite solutions (5.69) (magenta dotted lines) in each of panels (*a–c,e–f*).

$$\bar{S} = \sqrt{2W_{dry}^G \left(-X - \sqrt{\frac{D_0^{eff}}{\mathcal{A}(1-\nu)}} \left(1 - \exp\left(\sqrt{\frac{\mathcal{A}(1-\nu)}{D_0^{eff}}} X \right) \right) \right)} \quad \text{for } X \leqslant 0. \quad (5.65)$$
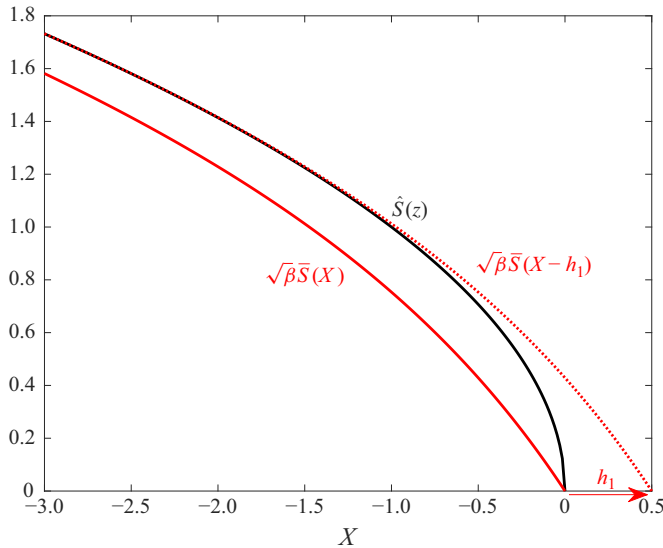
Figure 10. Schematic showing the matching between the outer (wet) and transition-layer regions. While $\sqrt{\beta}\bar{S}(X)$ and $\hat{S}(z)$ from (5.66) and (5.67) match at leading order, the constant translation of h_1 in X improves the agreement. (This is not a formal $O(\beta)$ correction, which would require higher order terms in the expansions of $\bar{S}$ and $\hat{S}$ in each region).

In particular, we see that the gradient $\bar{S}_X > 0$ at $X = 0$ is finite at the drying front, unlike the outer (wet) problem solution $\hat{S}$.

We note that

$$\sqrt{\beta}\bar{S} \sim \sqrt{\beta}\sqrt{2W_{dry}^G\left(-X - \sqrt{\frac{D_0^{eff}}{\mathcal{A}(1-\nu)}}\right)} \quad \text{as } X \to -\infty, \tag{5.66}$$

while from the boundary condition (5.62c) on the wet problem,

$$\hat{S} \sim \sqrt{2W_{dry}^G(h-z)} \quad \text{as } z \to h. \tag{5.67}$$

While (by construction, since $z = h + \beta X$) these clearly match to leading order, there is a discrepancy arising from the constant term in (5.66). This is illustrated schematically in figure 10. This discrepancy therefore motivates a shift of the transition-layer variable, replacing X by $X - h_1$, where

$$h_1 = \sqrt{\frac{D_0^{eff}}{\mathcal{A}(1-\nu)}} \tag{5.68}$$

may be viewed as a (constant) $O(\beta)$ correction to the drying front position h, and is chosen so that the limiting behaviours (5.66) and (5.67) fully agree (as shown in figure 10). We note that this is not a formal $O(\beta)$ correction to the interface position h, which would require going to higher order in both the wet and transition-layer regions, and a more careful matching. Nevertheless, using this shift in X, we may define composite solutions (by summing the inner (transition layer) and outer (wet region) solutions, and subtracting

Size of S	Drying stage	Time scale	Net evaporation rate scale	Reduced model	Composite solution
$S \gg Pe^{-1/2n}Ca^{1/n}$	Stage 1	$Pe^{1/2}$	$Pe^{-1/2}$	(5.24)	(5.27)
$S = O(Pe^{-1/2n}Ca^{1/n})$ so $k^L p_c = O(Ca\,Pe^{-1/2})$	Transition point	—	—	(5.34)	—
$S = O(Pe^{-1/n}Ca^{1/n})$	Stage 2	$Pe^{1-1/n}Ca^{1/n}$	Pe^{-1}	(5.58)	(5.69)

Table 3. Summary of our $Pe \gg 1$ analysis for the different stages of the drying process. Here, $k^L(S)p_c(S) \sim S^n$ as $S \to 0$.

the common limit), valid throughout the domain $z \in (0, 1)$,

$$h^{comp}(T) = h(T) + \beta h_1, \tag{5.69a}$$

$$S^{comp}(z, T) = \begin{cases} \eta\left(\hat{S}(z, T) + \sqrt{\beta}\sqrt{2W_{dry}^G\left(-\dfrac{z-h}{\beta} + h_1 \exp\left(\dfrac{z-h}{\beta h_1} - 1\right)\right)} \\ \quad -\sqrt{2W_{dry}^G(h-z)}\right) & \text{for } z < h^{comp}, \\ 0 & \text{for } z > h^{comp}, \end{cases} \tag{5.69b}$$

$$\rho^{comp}(z, T) = \begin{cases} 1 - \beta\dfrac{W_{dry}^G}{\mathcal{A}h_1}\exp\left(\dfrac{z-h}{\beta h_1}\right) & \text{for } z < h^{comp}, \\ \dfrac{1}{\nu}\left(1 - (1 - \nu\rho_\infty)\left(\dfrac{1-\nu}{1-\nu\rho_\infty}\right)^{\frac{1-z}{1-h}}\right) & \text{for } z > h^{comp}, \end{cases} \tag{5.69c}$$

$$U^{L,comp} = \begin{cases} Pe^{-1}\left(-\hat{S}\hat{S}_z - W_{dry}^G\exp\left(\dfrac{z-h}{\beta h_1} - 1\right)\right) & \text{for } z < h^{comp}, \\ 0 & \text{for } z > h^{comp}, \end{cases} \tag{5.69d}$$

$$U^{G,comp} = \begin{cases} Pe^{-1}W_{dry}^G\exp\left(\dfrac{z-h}{\beta h_1} - 1\right) & \text{for } z < h^{comp}, \\ Pe^{-1}W_{dry}^G & \text{for } z > h^{comp}. \end{cases} \tag{5.69e}$$

Here, $\hat{S}(z, T)$ and $h(T)$ are the solution of the wet-region problem (5.62), W_{dry}^G is as given by (5.50a) (evaluated at $h(T)$), and we have used the definition (5.68) of h_1 to simplify the notation. (We have not applied the shift of h_1 for ρ^{comp} in (5.69c) for the composite solution to remain continuous.)

These composite solutions are plotted as magenta dotted curves in figure 9. We see in figure 9(b) that our *ad hoc* correction h_1 is good early in stage 2, but does not capture the correction fully at later times. Nevertheless, the composite solutions S^{comp}, $U^{L,comp}$, ρ^{comp} and $U^{G,comp}$ capture the profiles very well in figure 9(a,c,e,f), respectively, with the best agreement at earlier times (carrying through from the fact that h^{comp} is most accurate at earlier times).

5.4. *Summary of the drying stages*

In table 3, we summarise our analysis of the limit $Pe \gg 1$. During stage 1, the saturation is uniform since capillary forces dominate, drawing liquid to the surface of the porous

medium, with evaporation only occurring in a thin $O(\sqrt{Pe})$ layer at the surface. The transition to stage 2 is reached when viscous drag limits the capillary flow of liquid; our (under) estimate is defined as the time where S becomes small enough for capillary and viscous forces to balance. This occurs at the critical saturation scaling of $S = O(Pe^{-1/2n}Ca^{1/n})$. Subsequently, in stage 2, we found a receding drying front at $z = h$, with evaporation only taking place within a thin layer at this front. The net evaporation rate is determined by the vapour transport from the front to the surface, and capillary forces pull liquid to the front, slowing its retreat. Since capillary forces are reduced over time as S becomes smaller, the receding front velocity increases over time.

6. Discussion and conclusions

Starting from an averaged continuum model of drying porous media, we have systematically derived a simpler reduced model for each of the two distinct stages of drying, in the limit of $Pe \gg 1$. Solutions of our reduced models were seen to accurately capture the behaviour of the full model, and give excellent qualitative agreement with experimental results in the literature. Important future work will be to compare quantitatively between our reduced models and experimental measurements. The main difficulty with such a comparison will be in quantifying the appropriate constitutive laws required. During stage 1, we showed that the crucial constitutive laws are the liquid–gas interfacial area and the effective vapour diffusivity. To predict the transition time and stage-2 behaviour, we also require accurate constitutive laws for the capillary pressure and liquid relative permeability.

In this limit of $Pe \gg 1$, for which the removal of vapour by diffusion is much slower than local vaporisation, we showed that the majority of the porous medium is at local equilibrium, with the vapour at its saturation point if there is liquid present locally. However, we found thin non-equilibrium regions (boundary or transition layers) in which the vapour density necessarily deviated from its saturation value for evaporation to occur there.

The reduced models that we have derived are much simpler and less expensive to simulate than the full model of Whitaker (1977) and, as a single ordinary or partial differential equation, are of a similar level of computational complexity to many phenomenological or simplified models used in the drying literature. Similarly to our stage-1 reduced model, Huinink, Pel & Michels (2002) proposed a stage-1 solution with a uniform saturation profile and a corresponding liquid flux linear in the spatial variable z (this model was also used by Guglielmini *et al.* (2008)). We have found the same structure through our systematic asymptotic analysis and, furthermore, quantified the net evaporation rate, flow rates and behaviour at the surface of the porous medium through matching with our boundary-layer region. Moreover, by carefully analysing the break-down of our stage-1 model as the saturation becomes small, we have predicted the time of the transition to stage 2. Our stage-2 reduced model for the saturation in the wet region is reminiscent of the phenomenological moisture-transport models used in the drying literature (Vu & Tsotsas 2018), with a similar nonlinear diffusion equation. However, our stage-2 model is defined on the shrinking wet domain as the drying front recedes into the porous medium, and our saturation-dependent diffusivity here is due to the capillary forces on the liquid. Furthermore, by coupling our stage-2 liquid-transport model to the vaporisation through the transition layer at the drying front and the vapour transport out of the porous medium, we predict the evolution of the receding front and the falling net evaporation rate.

One key finding from our analysis is that the choice of constitutive laws are critical to accurate modelling of the drying system via both our reduced models and with

averaged continuum models more generally. Specifically, we saw that for certain seemingly reasonable forms of the relative permeability, k^L, and capillary pressure, p_c, the model does not predict a transition to stage-2 drying, since, for those constitutive relations, the viscous drag does not dominate over the capillary forces as the saturation decreases. Additionally, we saw that the net drying rate during stage 1 was proportional to the square root of the product of the liquid–gas interfacial surface area and the effective diffusivity of vapour through the drying material, $\sqrt{\mathcal{A}D^{eff}}$. The variation of these constitutive relations with the saturation therefore determines whether the net evaporation rate rises, falls or is truly constant during stage 1. In practice, it is often difficult to accurately quantify the constitutive laws for realistic porous materials. Investigating the sensitivity of any drying model solution to the choice of constitutive laws is therefore important to build confidence in the model predictions. We emphasise that the solution is not sensitive to all constitutive laws, primarily only the two groups $\sqrt{\mathcal{A}D^{eff}}$, which determines the stage-1 drying rate, and $k^L p_c$, which determines when (or if) stage 1 transitions to stage 2.

We have presented a rigorous modelling framework through which to understand the drying of porous media. In addition to the parameter regime considered in this paper, our full dimensionless drying model of § 2 could be used to study other relevant parameter regimes. For instance, we might consider the case of higher capillary numbers, for which capillary forces do not dominate and we would expect a different receding-drying-front behaviour. Another highly relevant case is that of non-zero Bond number, where capillary forces must compete with gravity as well as viscous drag to draw liquid to the surface. In such cases, the stage 1–2 transition is observed to occur when the unsaturated region reaches some critical depth below the surface of the medium (Lehmann, Assouline & Or 2008; Shokri & Or 2011). We anticipate that similar asymptotic analyses to the present $Pe \gg 1$ case may provide valuable insight into these alternative drying regimes, and reduced models might be derived.

An important application of this work is to the transport and accumulation of impurities in the drying liquid, such as salt wicking, and weathering of rock and conservation of building materials (Oguchi & Yu 2021), as well as the accumulation of dirt within drying filters and textiles (Ji & Sanaei 2023; Luckins *et al.* 2024). We expect large Pe in these applications: for a filter membrane with $L \approx 10^{-3}$ m and $d \approx 10^{-6}$ m (and the data in table 1), we compute $Pe = 10^2$, while for a few centimetres of brick with $L \approx 10^{-2}$ m and $d \approx 10^{-6}$ m, we have $Pe = 10^4$. Capillary flows during drying draw impurities towards the surface of the porous medium and the accumulation of these impurities is also expected to impact on the drying behaviour (Gupta *et al.* 2014). The reduced models we have derived in the large-Pe limit are therefore a powerful tool with which to study the impurity transport problem, and our analysis could furthermore be extended to investigate the effect of accumulating impurities or salt crystals on the drying process, within the broad modelling framework presented in this paper.

REFERENCES

AHMAD, F., TALBI, M., PRAT, M., TSOTSAS, E. & KHARAGHANI, A. 2020 Non-local equilibrium continuum modeling of partially saturated drying porous media: comparison with pore network simulations. *Chem. Engng Sci.* **228**, 115957.

BEAR, J. 2013 *Dynamics of Fluids in Porous Media*. Courier Corporation.

BLUNT, M.J. 2017 *Multiphase Flow in Permeable Media: A Pore-Scale Perspective*. Cambridge University Press.

BRUNA, M. & CHAPMAN, S.J. 2015 Diffusion in spatially varying porous media. *SIAM J. Appl. Maths* **75** (4), 1648–1674.

FOWLER, A.C. 2011 *Mathematical Geoscience*, vol. 36. Springer.

GUGLIELMINI, L., GONTCHAROV, A., ALDYKIEWICZ, A.J. & STONE, H.A. 2008 Drying of salt solutions in porous materials: intermediate-time dynamics and efflorescence. *Phys. Fluids* **20** (7), 077101.

GUPTA, S., HUININK, H.P., PRAT, M., PEL, L. & KOPINGA, K. 2014 Paradoxical drying of a fired-clay brick due to salt crystallization. *Chem. Engng Sci.* **109**, 204–211.

HALL, C. & HOFF, W.D. 2021 *Water Transport in Brick, Stone and Concrete*. CRC Press.

HERTZ, H. 1882 Ueber die Verdunstung der Flüssigkeiten, insbesondere des Quecksilbers, im luftleeren Raume. *Annalen der Physik* **253** (10), 177–193.

HUININK, H.P., PEL, L. & MICHELS, M.A.J. 2002 How ions distribute in a drying porous medium: a simple model. *Phys. Fluids* **14** (4), 1389–1395.

HUPPERT, H.E. & WOODS, A.W. 1995 Gravity-driven flows in porous layers. *J. Fluid Mech.* **292**, 55–69.

JI, H. & SANAEI, P. 2023 Mathematical model for filtration and drying in filter membranes. *Phys. Rev. Fluids* **8** (6), 064302.

LASSEUX, D. & VALDÉS-PARADA, F.J. 2022 A macroscopic model for immiscible two-phase flow in porous media. *J. Fluid Mech.* **944**, A43.

LEHMANN, P., ASSOULINE, S. & OR, D. 2008 Characteristic lengths affecting evaporative drying of porous media. *Phys. Rev. E* **77** (5), 056309.

LI, Z., VANDERBORGHT, J. & SMITS, K.M. 2019 Evaluation of model concepts to describe water transport in shallow subsurface soil and across the soil–air interface. *Transport Porous Med.* **128** (3), 945–976.

LIU, Y., ZHENG, Z. & STONE, H.A. 2017 The influence of capillary effects on the drainage of a viscous gravity current into a deep porous medium. *J. Fluid Mech.* **817**, 514–559.

LOCKINGTON, D.A., PARLANGE, J.Y. & LENKOPANE, M. 2007 Capillary absorption in porous sheets and surfaces subject to evaporation. *Trans. Porous Med.* **68** (1), 29–36.

LUCKINS, E.K., BREWARD, C.J.W., GRIFFITHS, I.M. & PLEASE, C.P. 2023 A homogenised model for the motion of evaporating fronts in porous media. *Eur. J. Appl. Maths* **34** (4), 806–837.

LUCKINS, E.K., BREWARD, C.J.W., GRIFFITHS, I.M. & PLEASE, C.P. 2024 Mathematical modelling of impurity deposition during evaporation of dirty liquid in a porous material. *J. Fluid Mech.* **986**, A31.

METZGER, T. & TSOTSAS, E. 2010 Network models for capillary porous media: application to drying technology. *Chemie Ingenieur Technik* **82** (6), 869–879.

MURPHY, S. 2024 Mathematical modelling of chemical decontamination by cleanser solution and contamination of porous media contamination and decontamination models. PhD thesis. University of Limerick.

NORDBOTTEN, J.M. & CELIA, M.A. 2006 Similarity solutions for fluid injection into confined aquifers. *J. Fluid Mech.* **561**, 307–327.

NUSKE, P., JOEKAR-NIASAR, V. & HELMIG, R. 2014 Non-equilibrium in multiphase multicomponent flow in porous media: an evaporation example. *Intl J. Heat Mass Transfer* **74**, 128–142.

OGUCHI, C.T. & YU, S. 2021 A review of theoretical salt weathering studies for stone heritage. *Prog. Earth Planet. Sci.* **8** (1), 1–23.

OR, D., LEHMANN, P., SHAHRAEENI, E. & SHOKRI, N. 2013 Advances in soil evaporation physics – a review. *Vadose Zone J.* **12** (4), 1–16.

OUEDRAOGO, F., CHERBLANC, F., NAON, B. & BÉNET, J.-C. 2013 Water transfer in soil at low water content. Is the local equilibrium assumption still appropriate? *J. Hydrol.* **492**, 117–127.

PEL, L., BROCKEN, H. & KOPINGA, K. 1996 Determination of moisture diffusivity in porous media using moisture concentration profiles. *Intl J. Heat Mass Transfer* **39** (6), 1273–1280.

PEL, L. & LANDMAN, K.A. 2004 A sharp drying front model. *Dry. Technol.* **22** (4), 637–647.

PERRÉ, P., RÉMOND, R., ALMEIDA, G., AUGUSTO, P. & TURNER, I. 2023 State-of-the-art in the mechanistic modeling of the drying of solids: a review of 40 years of progress and perspectives. *Dry. Technol.* **41** (6), 817–842.

PERRÉ, P. & TURNER, I.W. 1999 A 3-D version of TransPore: a comprehensive heat and mass transfer computational model for simulating the drying of porous media. *Intl J. Heat Mass Transfer* **42** (24), 4501–4521.

PRAT, M. 2002 Recent advances in pore-scale models for drying of porous media. *Chem. Engng J.* **86** (1–2), 153–164.

PRAT, M. 2011 Pore network models of drying, contact angle, and film flows. *Chem. Engng Technol.* **34** (7), 1029–1038.

RICHARDS, L.A. 1931 Capillary conduction of liquids through porous mediums. *J. Appl. Phys.* **1** (5), 318–333.

SCHERER, G.W. 1990 Theory of drying. *J. Am. Ceram. Soc.* **73** (1), 3–14.

SHAMPINE, L.F. & REICHELT, M.W. 1997 The MATLAB ODE suite. *SIAM J. Sci. Comput.* **18** (1), 1–22.

SHOKRI, N. & OR, D. 2011 What determines drying rates at the onset of diffusion controlled stage-2 evaporation from porous media? *Water Resour. Res.* **47** (9), W09513.

TALBI, M. & PRAT, M. 2021 Coupling between internal and external mass transfer during stage-1 evaporation in capillary porous media: interfacial resistance approach. *Phys. Rev. E* **104** (5), 055102.

VAN GENUCHTEN, M.T. 1980 A closed-form equation for predicting the hydraulic conductivity of unsaturated soils. *Soil Sci. Soc. Am. J.* **44** (5), 892–898.

VU, H.T. & TSOTSAS, E. 2018 Mass and heat transport models for analysis of the drying process in porous media: a review and numerical implementation. *Intl J. Chem. Engng* **2018**, 1–13.

WEI, C.K., DAVIS, H.T., DAVIS, E.A. & GORDON, J. 1985 Heat and mass transfer in water–laden sandstone: convective heating. *Aiche J.* **31** (8), 1338–1348.

WHITAKER, S. 1977 Simultaneous heat, mass, and momentum transfer in porous media: a theory of drying. In *Advances in Heat Transfer*, vol. 13, pp. 119–203. Elsevier.

WU, R. & PRAT, M. 2022 *Mass Transfer Driven Evaporation from Capillary Porous Media*. CRC Press.